Article

Development of the first low nanomolar Liver Receptor Homolog-1 agonist through structure-guided design

Suzanne Mays, Autumn R. Flynn, Jeffery Cornelison, C. Denise Okafor, Hongtao Wang, Guohui Wang, Xiangsheng Huang, Heather Donaldson, Elizabeth Millings, Rohini Polavarapu, David Moore, John Calvert, Nathan T. Jui, and Eric A. Ortlund

Just Accepted

Development of the first low nanomolar Liver Receptor Homolog-1 agonist through structure-guided design

Suzanne G. Mays[1], Autumn R. Flynn[2], Jeffery L. Cornelison[2], C. Denise Okafor[1], Hongtao Wang[4], Guohui Wang[4], Xiangsheng Huang[4], Heather N. Donaldson[1], Elizabeth J. Millings[1,3], Rohini Polavarapu[3], David D. Moore[5], John W. Calvert[3], Nathan T. Jui[2], and Eric A. Ortlund[1]*

1. Department of Biochemistry, Emory University School of Medicine, Atlanta, Georgia 30322, USA

2. Department of Chemistry, Emory University, Atlanta, Georgia 30322, USA

3. Department of Surgery, Carlyle Fraser Heart Center, Emory University, Atlanta, Georgia 30322, USA

4. Department of Pediatrics, Section of Gastroenterology, Baylor College of Medicine and Texas Children's Hospital, Houston, Texas 77030, USA

5. Department of Molecular and Cell Biology, Baylor College of Medicine, Houston, Texas 77030, USA

ABSTRACT

As a key regulator of metabolism and inflammation, the orphan nuclear hormone receptor, Liver Receptor Homolog-1 (LRH-1), has potential as a therapeutic target for diabetes, nonalcoholic fatty liver disease, and inflammatory bowel diseases. Discovery of LRH-1 modulators has been difficult, in part due to the tendency for synthetic compounds to bind unpredictably within the lipophilic binding pocket. Using a structure-guided approach, we exploited a newly-discovered polar interaction to lock agonists in a consistent orientation. This enabled the discovery of the first low nanomolar LRH-1 agonist, one hundred times more potent than the best previous modulator. We elucidate a novel mechanism of action that relies upon specific polar interactions deep in the LRH-1 binding pocket. In an organoid model of inflammatory bowel disease, the new agonist increases expression of LRH-1-conrolled steroidogenic genes and promotes anti-inflammatory gene expression changes. These studies constitute major progress in developing LRH-1 modulators with potential clinical utility.

INTRODUCTION

Liver Receptor Homolog-1 (LRH-1; NR5A2) is a nuclear hormone receptor (NR) that is highly expressed in the liver and tissues of endodermal origin. It is indispensable during embryonic development, where it plays a role in maintenance of pluripotency[1], as well as in the development of the liver and pancreas[2]. In adults, LRH-1 controls diverse transcriptional programs in different tissues related to metabolism, inflammation, and cellular proliferation. Targeted metabolic pathways include bile acid biosynthesis[3], reverse cholesterol transport[4-5], *de novo* lipogenesis[6-7], and glucose phosphorylation and transport[8-9]. The ability to modulate lipid and glucose metabolism suggests therapeutic potential for LRH-1 agonists in metabolic diseases such

as nonalcoholic fatty liver disease, type II diabetes, and cardiovascular disease. Indeed, the phospholipid LRH-1 agonist dilauroylphosphatidylcholine (DLPC; PC 12:0/12:0) improves glucose tolerance, insulin sensitivity, and triglyceride levels in obese mice[6]. These anti-diabetic effects occur in an LRH-1-dependent manner and have been primarily attributed to a reduction of *de novo* lipogenesis[6]. In addition, targeting LRH-1 in the gut has therapeutic potential for inflammatory bowel disease, where LRH-1 overexpression ameliorates disease-associated inflammation and cell death[10].

While small molecule LRH-1 modulators are highly sought, the large and lipophilic LRH-1 binding pocket has been extremely challenging to target. A promising class of agonists developed by Whitby and colleagues features a bicyclic hexahydropentalene core scaffold[11-12]. The best-studied of this class, named RJW100, was discovered as a part of an extensive synthetic effort to improve acid stability and efficacy of a related compound, GSK8470[12] (Figure 1A). We recently determined the crystal structure of LRH-1 bound to RJW100 and made a surprising discovery: it exhibits a completely different binding mode than GSK8470, such that the bicyclic cores of the two agonists are perpendicular to each other (Figure 1A)[13]. As a result, the two compounds use different mechanisms to activate LRH-1 but exhibit similar activation profiles in luciferase reporter assays[13]. A tendency for ligands in this class to bind unpredictably in the hydrophobic pocket has likely been a confounding factor in agonist design. However, insights from the LRH-1-RJW100 structure have provided new strategies to improve activity.

In the LRH-1-RJW100 crystal structure, the ligand *exo* hydroxyl group contacts a network of water molecules deep in the ligand binding pocket (Figure 1B). This water network coordinates a small group of polar residues (*e.g.* Thr352, His390, and Arg393) in an otherwise predominantly
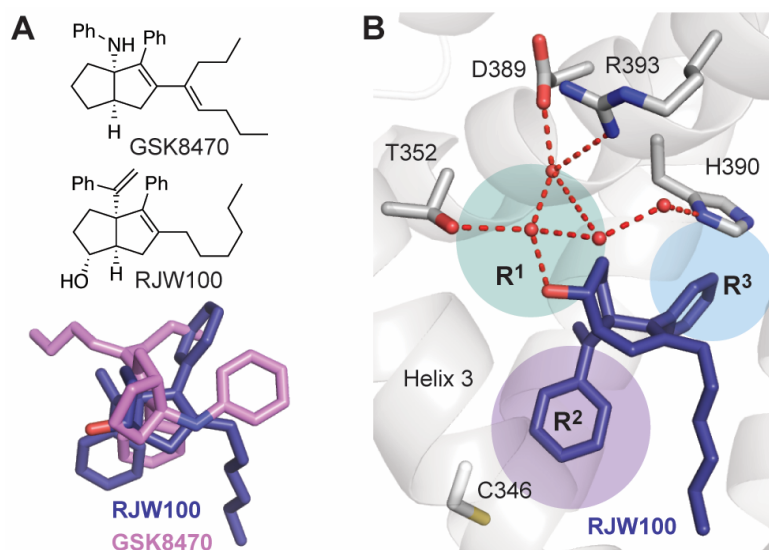
Figure 1. Structure-based design of LRH-1 agonists. A. Top, chemical structures of the agonists GSK8470 and RJW100. Bottom, superposition of GSK8470 and RJW100 (from PDB 3PLZ and 5L11, respectively)[12-13] show the very different binding modes for these similar agonists. B. RJW100 interacts with LRH-1 residue Thr352 via water. The four water molecules shown coordinate a group of polar residues deep in the binding pocket. The colored circles indicate the areas targeted by modifications to the RJW100 scaffold in this work.

hydrophobic pocket. The *endo* RJW100 diastereomer adopts a nearly identical pose and makes the same water-mediated contact with Thr352, supporting the idea that this interaction is a primary driver of ligand orientation[13]. Using both a RJW100 analog lacking a hydroxyl group and a LRH-1 Thr352Val mutation, we demonstrated that this interaction is required for RJW100-mediated activation of LRH-1[13]. As the basis for the current studies, we hypothesized that strengthening this and other polar interactions in the vicinity could anchor ligand conformation, enabling more predictable targeting of desired parts of the pocket. We designed, synthesized, and evaluated novel compounds around the hexahydropentalene scaffold with the primary aim of strengthening polar contacts in the deep part of the binding pocket (the deep part of the pocket is hereafter abbreviated "DPP"). This systematic, structure-guided approach enabled the discovery of an agonist more

potent than RJW100 by two orders of magnitude in luciferase reporter assays. We present three crystal structures of LRH-1 bound to novel agonists, which depict the modified polar groups projecting into the DPP. The best new agonist modulates expression of LRH-1-controlled anti-inflammatory genes in intestinal organoids, suggesting therapeutic potential for treating inflammatory bowel diseases. This breakthrough in LRH-1 agonist development is a crucial step in developing potential new treatments for metabolic and inflammatory diseases.

RESULTS

Locking the agonist in place with polar interactions. Our structural studies have revealed that highly similar LRH-1 synthetic agonists can bind unpredictably within the hydrophobic binding pocket, which has presented a challenge for improving agonist design in a rational manner[13]. We reasoned that strengthening contacts within the DPP may anchor synthetic compounds in a consistent orientation and improve potency. To evaluate this hypothesis, we synthesized RJW100 analogs with bulkier polar groups in place of the RJW100 hydroxyl (R^1), aiming to displace bridging waters and to generate direct interactions with Thr352 or other nearby polar residues (Figure 1B). In parallel, we synthesized compounds designed to interact with other sites in the DPP by (1) modifying the external styrene (R^2) to promote interactions with helix 3 or to fill a hydrophobic pocket in the vicinity or (2) incorporating hydrogen bond donors at the *meta* position of the internal styrene (R^3) to promote hydrogen bonding with His390 (also via water displacement) (Figure 1B). To prepare this compound library, we utilized a diastereoselective variant of Whitby's zirconecene-mediated Pauson-Khand-type cyclization[14]. This highly modular approach unites three readily available precursors (an enyne, an alkyne, and 1,1 dibromoheptane) to generate all-carbon bridgehead [3.3.0]-bicyclic systems with varying functionality at positions R^1, R^2, and R^3 (Figure 2A). R^1 was most conveniently varied through

A

Whitby Cyclization
(one step)

Modification at OR
(R^2 = PhCCH$_2$, R^3 = Ph)

enyne   alkyne   1,1-dibromoheptane

R^1 : water displacement, deep pocket polar interactions (R^2 = PhCCH$_2$, R^3 = Ph)

(±) endo   1N   2N   3N   4N   5N   6N   7N   8N

(±) exo   1X   2X   3X   4X   5X   6X   7X   8X

B

R^2 : helix 3 interactions (R^1 = OH, *exo* only, R^3 = Ph)

9   10   11   12

13   14   15

R^3 : H-bond with His390 (R^1= OH, *exo* only, R^2 = PhCCH$_2$)

16   17   18   19

20   21   22   23

C

RJW100: R^1 = OH, *exo* only, R^2 = PhCCH$_2$, R^3 = Ph. EC$_{50}$ = 1.5 ± 0.4 μM, RE = 1.0

Endo Cmpd	1N	2N	3N	4N	5N	6N	7N	8N
EC$_{50}$ (μM)	i.a.	13 ± 8	i.a.	0.5 ± 0.7	0.9 ± 0.6	0.0157 ± 0.0008	1 ± 1	0.1 ± 0.2
RE	i.a.	2.6	i.a.	0.30	0.96	1.3	1.2	0.18
Exo Cmpd	1X	2X	3X	4X	5X	6X	7X	8X
EC$_{50}$ (μM)	i.a.	i.a.	i.a.	2 ± 3	0.8 ± 0.6	0.040 ± 0.005	i.a.	i.a.
RE	i.a.	i.a.	i.a.	0.41	0.62	0.39	i.a.	i.a.

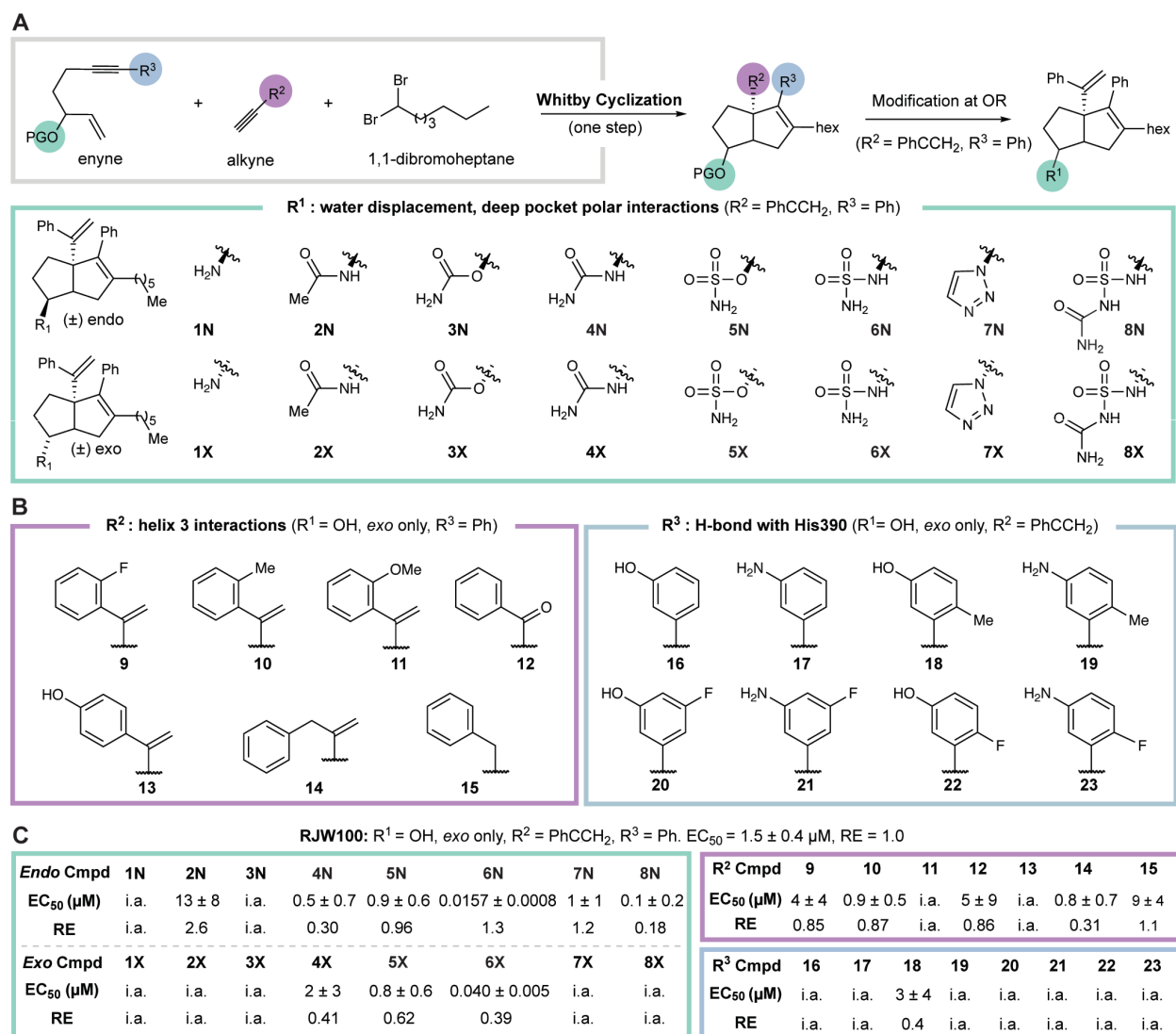| R^2 Cmpd	9	10	11	12	13	14	15
EC$_{50}$ (μM)	4 ± 4	0.9 ± 0.5	i.a.	5 ± 9	i.a.	0.8 ± 0.7	9 ± 4
RE	0.85	0.87	i.a.	0.86	i.a.	0.31	1.1
R^3 Cmpd	16	17	18	19	20	21	22	23
EC$_{50}$ (μM)	i.a.	i.a.	3 ± 4	i.a.	i.a.	i.a.	i.a.	i.a.
RE	i.a.	i.a.	0.4	i.a.	i.a.	i.a.	i.a.	i.a.

Figure 2. Synthesis of LRH-1-targeted compounds. A. Overview of synthetic strategy used to generate agonists based on modification of the [3.3.0]-bicyclic hexahydropentalene scaffold. B. Modifications to the scaffold evaluated in this study, grouped by site of modification by colored boxes. C. Summary of EC$_{50}$ and efficacy relative to RJW100 (RE). RE was calculated as described in the methods section. RJW100 RE = 1.0 and EC$_{50}$ = 1.5 +/- 0.4 μM. The abbreviation "i.a." refers to inactive compounds for which EC$_{50}$ values could not be calculated.

modification of the RJW100 alcohol to yield derivatives **1–8**, which were synthesized separately as both the *endo* (N) or *exo* (X) diastereomers (Figure 2B). Oxygen-linked analogs **3** and **5** were

formed directly from the diastereomerically-appropriate parent alcohol. Nitrogen-linked analogs

1, **2**, **4**, **6**, and **8** were prepared through alcohol activation (mesylate **S4**) and substitution (azide

S2, nitrile **S3**) (Figure 2B and online supplementary materials). Alteration of R^2 was

accomplished by introducing phenylacetylene derivatives as the alkyne in the cyclization step

(Figure 2A), generating **9–15** (Figure 2B). R^3 variants **16–23** were prepared using functionalized

enyne starting materials. Detailed chemical syntheses of all intermediates and tested compounds

are provided in the online supplementary materials.

Discovery of the first low nanomolar LRH-1 agonist. We evaluated the new compounds using

differential scanning fluorimetry (DSF), since entropic gain from displacement of buried water

molecules or favorable energetics from bond formation would result in global stabilization of the

LRH-1-agonist complex. DSF assays were paired with cellular luciferase reporter assays to

determine effects on LRH-1 transcriptional activity. Luciferase data are summarized in Figure 2C

and dose-response curves are shown in Figure S1.

As previously observed[13, 15], RJW100 stabilizes the LRH-1 ligand binding domain (LBD) by

around 3 ºC relative to a PL ligand in DSF assays (Figure 3A). While the R^2- and R^3-modified

compounds (**9-23**) destabilize the receptor relative to RJW100 (Figure 3A) and tend to be poor

activators (Figure 2C, S1), certain R^1 modifications are highly stabilizing, with T_m values 3-8 °C

higher than RJW100 (Figure 3A and online supplementary material). There is a striking

correlation between potency in luciferase reporter assays and LRH-1 stabilization by DSF for the

R^1-modified compounds, where lower EC_{50}s are associated with higher T_m values (Pearson

correlation coefficient = -0.71; p = 0.0009, Figure 3B). This correlation provides a direct link

between cellular activity and receptor stabilization. There is no correlation between T_m and EC_{50}
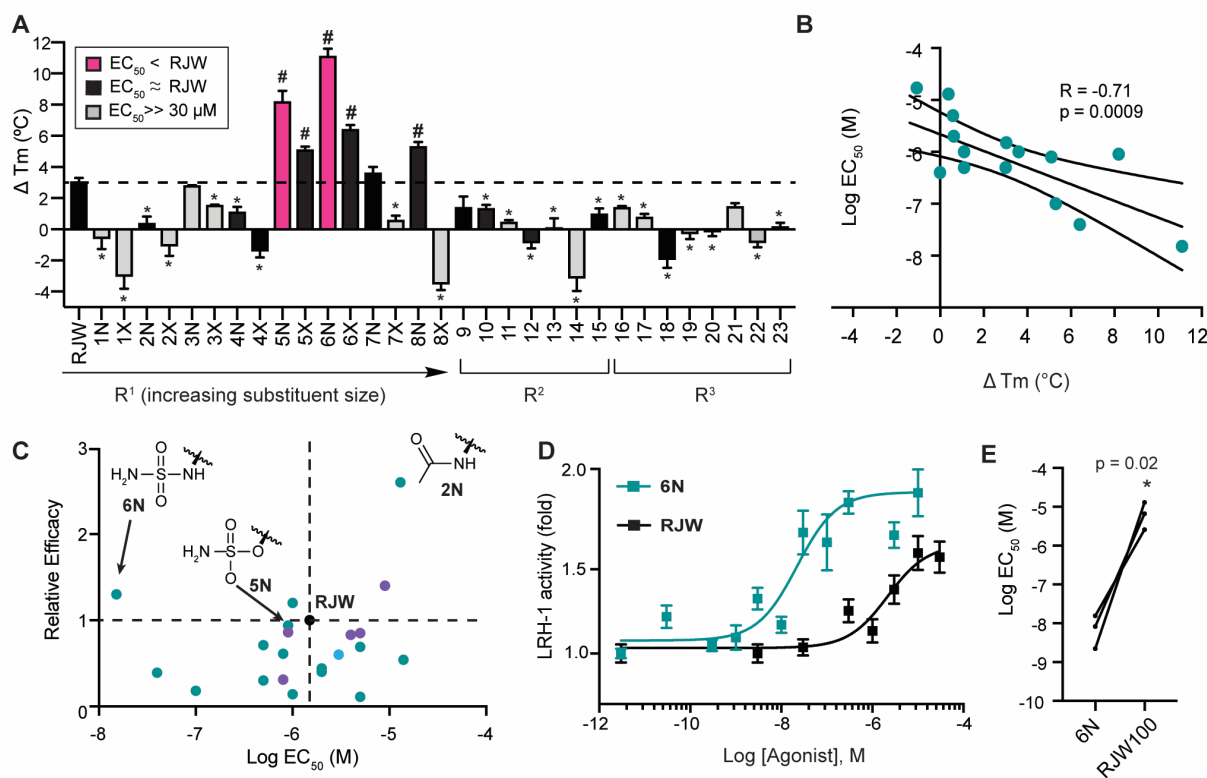
Figure 3. Optimization of R^1 modification improves potency by two orders of magnitude. A. DSF assays

demonstrate that the site of modification, R^1 substituent size, and stereochemistry affect global LRH-1 stabilization.

Colored bars represent EC_{50}s relative to RJW100 as indicated in the legend. Each bar represents three experiments

conducted in triplicate. *, $p < 0.05$ for T_m decrease *versus* RJW100. #, $p < 0.05$ T_m increase *versus* RJW100.

Significance was assessed by one-way ANOVA followed by Dunnett's multiple comparison's test. *Dotted line*

indicates the T_m change induced by RJW100 relative to the phospholipid agonist, DLPC. B. Scatter plot showing

the correlation between $T_{m.}$ shift in DSF assay (x-axis) and EC_{50} from luciferase reporter assays (y-axis) for the R^1-

modified compounds. Data were analyzed by linear regression (curved lines are the 95% confidence interval. C.

Scatter plot comparing potency (EC_{50}) and efficacy relative to RJW100 (relative efficacy, RE) for all compounds for

which EC_{50} values could be calculated. Dots are color-coded by site of modification (as indicated in Figure 2). The

black dot is RJW100. The EC_{50} values and efficacies of compounds **2N**, **5N**, and **6N** are indicated. Relative efficacy

was calculated as described in the methods section. D. Dose response curves comparing **6N** and RJW100 in

luciferase reporter assays. Each point represents the mean ± SEM for three experiments conducted in triplicate. E.

The significance of difference in potency for **6N** *versus* RJW100 was determined by a two-tailed, paired Student's t-

test from parallel experiments.

for the R^2- and R^3-modified compounds (data not shown), suggesting that improved potency is due to specific polar interactions mediated by the R^1 group.

The R^1 modifications are diverse, ranging from small to large polar groups, including hydrogen bond donors and acceptors and *endo* and *exo* diastereomers (Figure 2B). Both size and stereochemistry of the R^1 group are important for activity. Mid-sized polar groups, mainly tetrahedral in geometry, tend to increase potency relative to RJW100 (Figure 2C). The close relationship between R^1 size, agonist potency, and LRH-1 stabilization is evident looking at DSF results, where a strong peak in stabilization occurs for compounds **5 – 6** and **8N** (Figure 3A). Another strong trend among the data is that *endo* diastereomers are better activators (and more stabilizing) than the corresponding *exo* diastereomers (as seen for the triazoles **7,** sulfamides **6,** and acetamides **2**, Figure 2–3). While the compounds display a wide range of potencies and efficacies, the *endo* sulfamide (**6N**) stands out as being the most potent (Figure 3C). With an EC_{50} of 15 nM, **6N** is two orders of magnitude more potent than RJW100 (Figure 3D-E). This is the first discovery of a low-nanomolar LRH-1 modulator, representing a leap forward in developing agonists for this challenging target.

DPP contacts drive LRH-1 activation by 6N. The improved potency of **6N** is particularly striking considering that a very similar, highly stabilizing compound (**5N**) is not much more potent or effective for transcriptional activation than RJW100 (Figure 3C). The dramatic increase in potency for **6N** relative to **5N** is driven by replacement of oxygen with nitrogen in the R^1 linker, as this is the only difference between the two compounds. Remarkably, a nitrogen-containing linker improves potency relative to an oxygen linker for several pairs of compounds that differ only at this site (Figure 4A). The NH linker also contributes to selectivity for LRH-1 over its closest homolog, Steroidogenic Factor-1 (SF-1). Compound **6N** is a weaker activator of SF-1 than
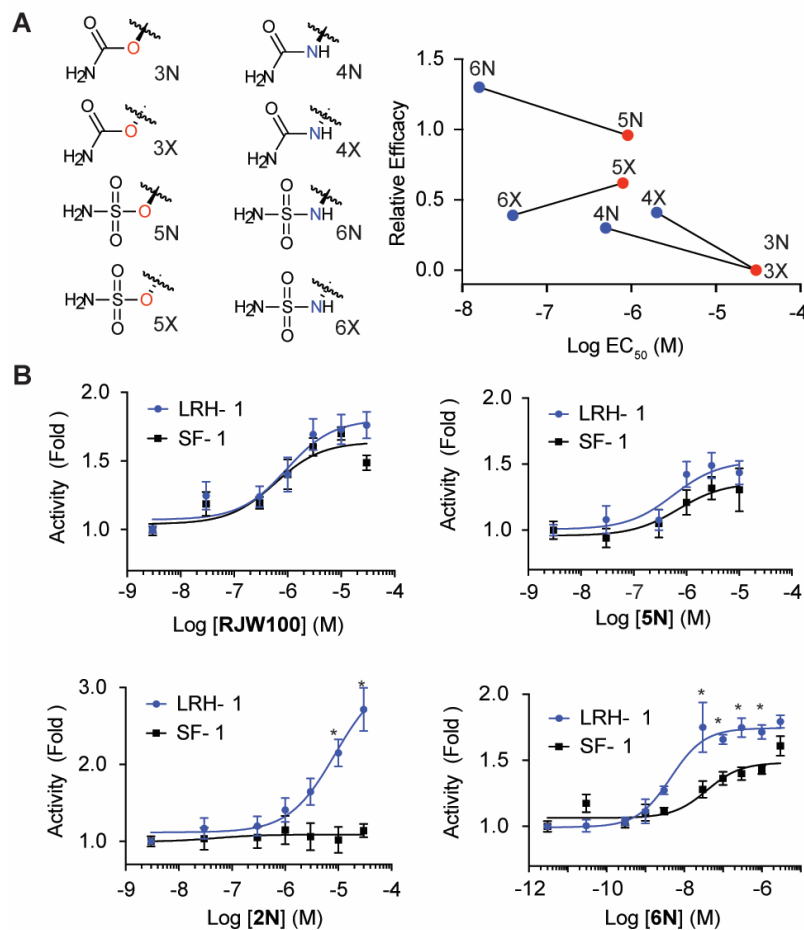
Figure 4. A hydrogen-bond donating nitrogen linker in the R^1 group improves potency and selectivity. A-B. Comparison of potencies and efficacies for four sets of compounds that are identical except for the presence of a R^1 linker containing an oxygen (red dots) or nitrogen (blue dots). Compounds with no activity at doses up to 30 µM are (**3N** and **3X**) are plotted as having EC_{50}s of 30 µM and Relative Efficacy of 0 for illustrative purposes. C. Dose response curves comparing activation of LRH-1 and SF-1 by select compounds. Significance of differences in activities of each compound for LRH-1 versus SF-1 was determined by two-way ANOVA followed by Sidak's multiple comparison's test. *, $p < 0.05$.

LRH-1, and **2N** (the *endo* acetamide) displays no activity against SF-1 while strongly activating LRH-1 (Figure 4C). In contrast, **5N** and RJW100 equally activate both receptors (Figure 4C).

To investigate the role of the R^1 linker in agonist activity and to gain insights into mechanisms underlying the potency of **6N**, we determined the X-ray crystal structure of **6N** bound to the LRH-1 LBD at a resolution of 2.23 Å (Figure 5A, Table S1). For comparison and to delineate the function of the NH-containing linker, we also determined structures of LRH-1 bound to **2N** (with an NH-linker, 2.2 Å) and **5N** (with an oxygen linker, 2.0 Å) (Table S1). The complexes were crystallized with a fragment of the coactivator protein, Transcriptional Intermediary Factor 2 (Tif2), which is bound at the AF-2 activation function surface (AFS) at the interface between helices 3, 4, and the activation function helix (AF-H, Figure 5A). Overall protein conformation does not differ greatly and is similar to the LRH-1-RJW100 structure (root mean square deviations are within 0.2 Å). The ligands are well-defined by the electron density, with the exception of the alkyl "tails" (Figure 5B). Disorder in the tail is also seen in the *endo* RJW100 structure[12] and may be a general feature of *endo* agonists with this scaffold.

One of the main goals for these studies was to develop ligands that bind with consistent positions of the bicyclic cores. These structures demonstrate that this strategy was successful. Superposition of RJW100, **2N 5N**, and **6N** from the crystal structures shows nearly identical conformation of the agonists' cores and phenyl groups, with slight variation in the positions of the R^1 headgroups (Figure 5C). All three headgroups protrude into the DPP, filling space typically occupied by one or more water molecules and making several polar contacts (Figure 5D). For both **5N** and **6N**, there is strong tetrahedral density indicating the position of the R^1 groups; however, analysis of structure B factors and ensemble refinement[16] suggest that the R^1 groups are somewhat mobile and capable of making transient interactions in the pocket that differ from the modeled states (Figure S3). Studies with LRH-1 mutants helped to elucidate mechanistic differences between these agonists.
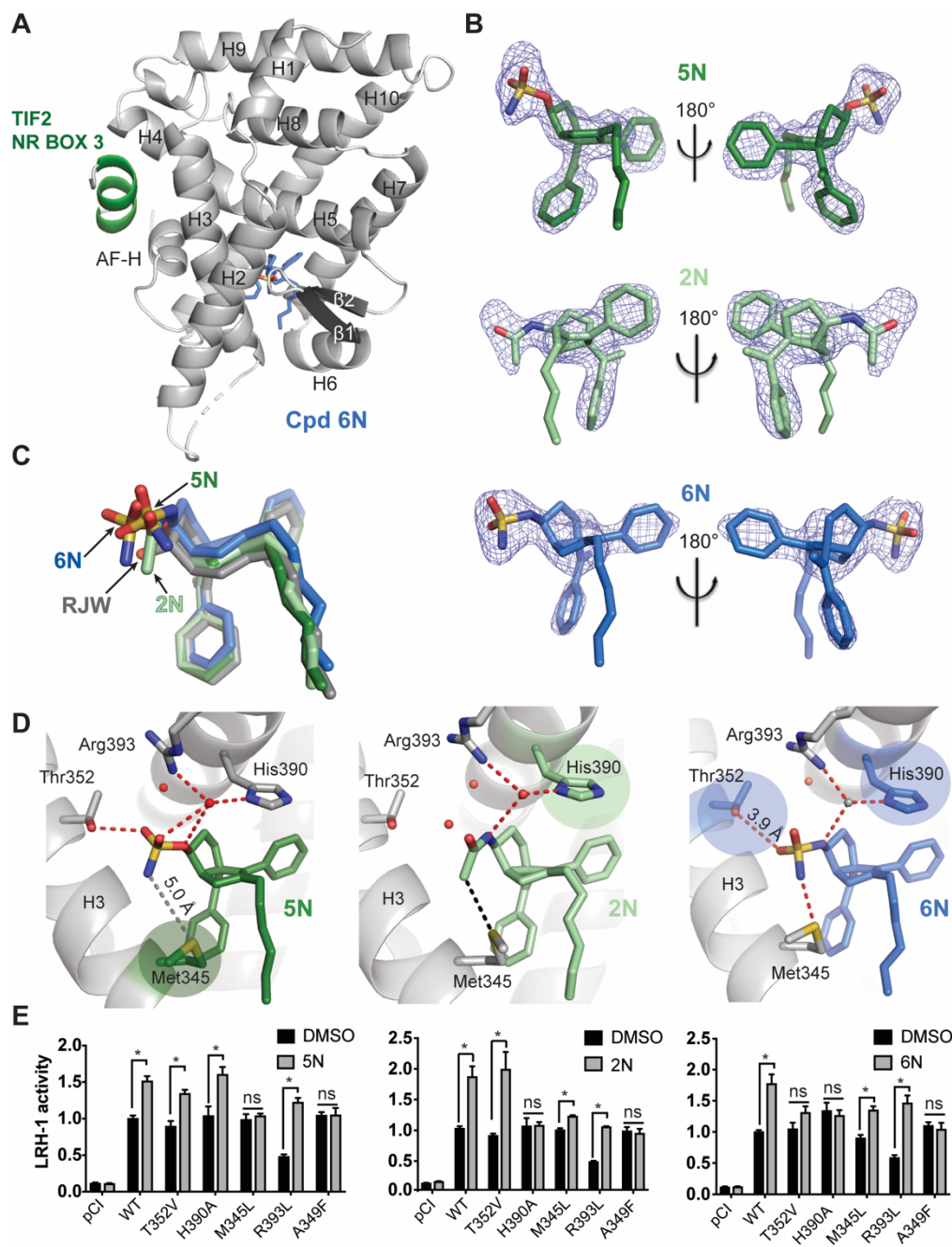
Figure 5. Crystal structures of LRH-1 bound to novel agonists. A. Overall structure of the LRH-1 LBD (grey) bound to **6N** (blue sticks). Tif2 is shown in green. The dotted line indicates a disordered region that could not be modeled. B. Omit maps for **2N**, **5N**, and **6N**. Maps are F_O-F_C, contoured at 2.5σ. C. Superposition of ligands from the crystal structures showing a consistent position of the cores of the modified agonists compared to RJW100. D. Close view of LRH-1 binding pocket with either **5N**, **2N**, or **6N** bound showing a subset of interactions made by the R^1 groups.

Colored circles highlight interactions that are important for LRH-1 activation by each agonist. Red spheres are water molecules (the grey sphere in the LRH-1-**6N** structure is a water molecule typically present in the LRH-1 pocket that could not be modeled due to poor crystallographic order). Red dotted lines indicate hydrogen bonds, and black dotted lines indicate hydrophobic contacts. The interaction indicated by the grey dotted line in the LRH-1-**5N** structure is outside of hydrogen-bonding distance in the structure but important for activity in mutagenesis studies. E. Luciferase reporter assays showing how the interactions made by the agonists affect LRH-1 activity. The A349F mutation occludes the DPP and was used as a negative control. Each bar represents the mean ± SEM for three independent experiments conducted in triplicate. Cells were treated with 10 μM **2N**, 10 μM **5N**, or 0.3 μM **6N** for 24 hours (concentrations chosen based on agonist EC_{50} toward wild-type LRH-1). *, $p < 0.05$ by two-way ANOVA followed by Dunnett's multiple comparisons test. PDB codes for the structures compared in this figure are as follows: LRH-1-**RJW100**, 5L11; LRH-1-**5N**, 6OQX; LRH-1-**6N**, 6OQY; LRH-1-**2N**, 6OR1.

While the binding modes of the three agonists are similar, mutagenesis studies show that they activate LRH-1 through different mechanisms (Figure 5E). The first major difference is with the Thr352 interaction. Both **5N** and **6N** directly interact with Thr352, but the differential impact of a Thr352Val mutation shows that this interaction only contributes to agonist-mediated LRH-1 activity in the case of **6N** (Figure 5E). Compound **2N** is not well-positioned to interact with the water coordinating Thr352 due to the planar geometry of the R^1 acetamide group, and the Thr352Val mutation has no effect on LRH-1 activity (Figure 5E). The agonists also demonstrate a differential reliance on the interaction with M345: **5N** is unable to activate a Met345L LRH-1 mutant, but **6N** and **2N** activate it significantly above basal levels (Figure 5E).

We were particularly interested in how interactions made by the NH linker contribute to agonist activity. All three agonists are positioned to make water-mediated hydrogen bonds with LRH-1 residue His390 via the R^1 linkers (Figure 5D). In the case of **6N**, we were unable to model the bridging water molecule seen in the other two structures (and in other published LRH-1 LBD

structures[13, 15, 17-20]) due to weak electron density. The weak density for the water molecule is likely a consequence of poor crystallographic order, since very few waters could be modeled in this structure (24 total, unusual for a 2.2 Å structure). However, luciferase reporter assays with LRH-1 mutants indicate that **6N** interacts with His390 and that the interaction is critical for transcriptional activity (Figure 5E). Compound **2N** is also unable to activate the LRH-1 His390Ala mutant, supporting the idea that a productive water-mediated interaction with His390 is made by the NH-linker, (Figure 5E). Compound **5N**, with an oxygen linker, interacts with His390 with both the linker and sulfonyl oxygens (Figure 5D). However, **5N** does not utilize the His390 interaction for activation, since mutating His390 to alanine has no effect on its ability to activate LRH-1 (Figure 5E). Therefore, while **5N** and **6N** make very similar contacts, the presence of a hydrogen bond donor in the R^1 linker is uniquely able to drive activation of LRH-1 via His390. This provides a potential mechanism through which a nitrogen linker increases agonist potency.

Compound 6N stabilizes the AFS, strengthens allosteric signaling, and promotes coactivator recruitment. To investigate how **6N** alters LRH-1 dynamics to drive receptor activation, we determined its effects of LRH-1 conformation in solution using hydrogen-deuterium exchange (HDX) mass spectrometry. The most significant changes occur at sites involved in ligand-driven recruitment of coregulators: (1) the activation function surface (AFS) and (2) a region of the receptor involved in allosteric signaling to the AFS, located near helix 6 and the beta sheets[18-19] (this site is called activation function B and abbreviated "AF-B". Relative to RJW100, **6N** impacts the conformation of AF-B by destabilizing the N-terminal portion of helix 7 and stabilizing the loop between helices 6 and 7 (Figure 6A). Rigidification of the loop between these helices may induce pressure to unwind helix 7, which could explain this pattern of motion. In addition to these changes near AF-B, **6N** strongly stabilizes a portion of helix 4 near the AFS (Figure 6A).
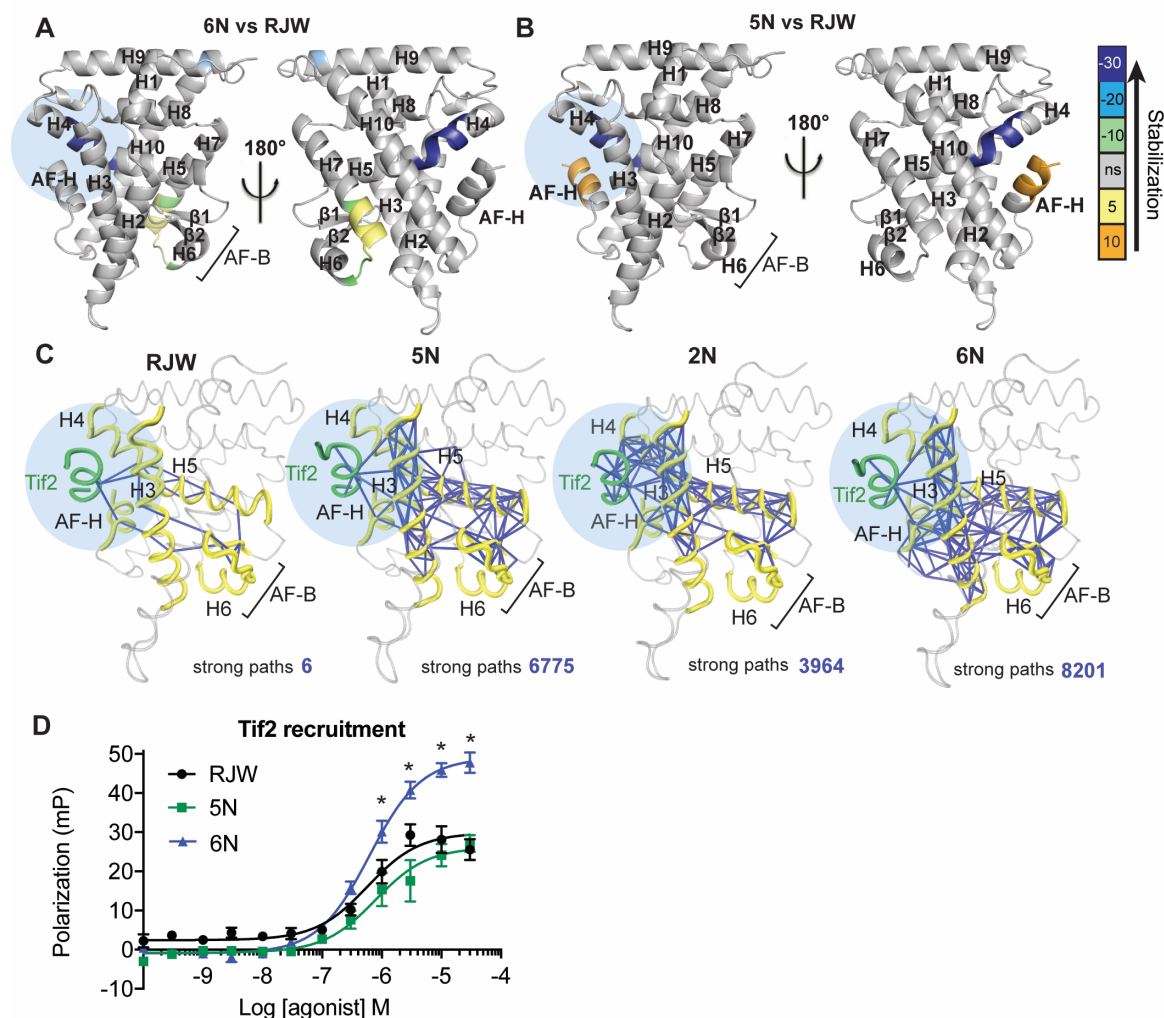
Figure 6. Compound 6N promotes allosteric communication to the AFS and coactivator recruitment. A-B. Differential HDX comparing **5N** to RJW100 (*A*) or **6N** to RJW100 (*B*). Color bar indicates the percent difference in deuterium uptake when **5N** or **6N** is bound compared to RJW100. A positive number indicates more deuterium exchange, indicating relative destabilization. A negative number indicates relative stabilization. C. MDS results showing the strongest suboptimal paths (blue lines) between AF-B and the Tif2 coactivator (green) when the indicated agonists are bound. The AFS is highlighted in light blue in panels A-C, and the position of AF-B is indicated with brackets. The PBD codes for the starting models used in MD are: LRH-1-**RJW100**, 5L11; LRH-1-**5N**, 6OQX; LRH-1-**6N**, 6OQY; LRH-1-**2N**, 6OR1. D. Compound **6N** promotes recruitment of the Tif2 coactivator to purified LRH-1 LBD in a fluorescence polarization-based binding assay. Each point represents the mean +/- SEM for three independent experiments conducted in triplicate. *, $p < 0.05$ by two-way ANOVA followed by Sidak's multiple comparison's test.

Compound **5N** stabilizes the same region of helix 4 relative to RJW100 and **6N**, but it also destabilizes the AF-H, a critical part of the AFS that tunes coregulator associations through subtle changes to its conformation[19]. (Figure 6B).

Since **6N** alters LRH-1 conformation at AF-B and the AFS, we hypothesized that it increases communication between these two sites. To quantify the predicted strength of agonist-driven communication between AF-B and the AFS, we conducted 1 μs molecular dynamics simulations (MDS) using the crystal structures as starting models. Correlated motions of residues within a protein facilitate allosteric coupling between distant sites[21-23]. Communication paths can traverse thousands of possible routes through the receptor, and the chains of residues with the strongest patterns of correlated motion—the optimal path and a subset of suboptimal paths— are thought to convey the most information[24-25]. We therefore constructed dynamical networks of LRH-1-agonist complexes, using calculated covariance to weight the strength of communication between pairs of residues. The resulting covariance matrices were used to identify the strongest suboptimal paths facilitating communication between AF-B and Tif2 coactivator (bound at the AFS). The number of strong paths markedly increases when **2N**, **5N**, or **6N** are bound compared to RJW100, with **6N** exhibiting the strongest communication between these sites (Figure 6C). There are also significant differences in the directionality of the paths promoted by each agonist. Although all paths traverse helix 5, indicating that correlated motion is induced in this region, compounds **2N**, **5N**, and **6N** also induce strong communication along helix 3. Compound **6N** also induces highly interconnected communication within the AFS and the Tif2 coactivator, including significant involvement of the AF-H. This important helix in the AFS is notably excluded from the paths when the other agonists are bound (Figure 6C).

The stabilization of the AFS by **6N** is associated with enhanced coactivator recruitment. In a fluorescence-polarization based coregulator binding assay, RJW100, **5N**, and **6N** dose-dependently recruit fluorescein-labeled Tif2 peptide to LRH-1 and exhibit similar EC_{50}s (50% of maximum Tif2 binding occurs with ~600-700 nM agonist, Figure 6D). Each curve reaches a well-defined plateau that indicates the maximum response with saturating concentrations of agonist; however, curve maxima are lower for RJW100 and **5N** than **6N** by 50–60%, which is characteristic of partial agonists. Although the endogenous ligand has not been identified for comparison, **6N** behaves more like a full agonist than **5N** or RJW100 in this assay. Therefore, we have elucidated a novel mechanism of action utilized by **6N**, whereby specific interactions by the sulfamide and R^1 linker promote allosteric signaling to the AFS, stabilizing the site of coactivator interaction and increasing Tif2 association.

Compound 6N promotes expression of intestinal epithelial steroidogenic genes in humanized LRH-1 mouse enteroids. The discovery of the first highly potent LRH-1 agonist provides the opportunity to elucidate ligand-regulated transcriptional pathways controlled by this receptor. LRH-1 controls local steroid hormone production in the gut epithelium[26-27], and overexpression of LRH-1 reduces inflammatory damage in immunologic mouse models of enterocolitis[10]. These findings suggest therapeutic potential for LRH-1 agonists in inflammatory bowel diseases (IBD). The recent development of methods to culture organoids of intestinal crypts (enteroids, Figure 7A) has provided an excellent research tool for drug discovery for IBD[28]. When stimulated with inflammatory cytokines, enteroids mimic features of gut epithelia in IBD[10, 28]. To investigate anti-inflammatory properties of **6N**, we measured the effects of the new agonist on gene expression in
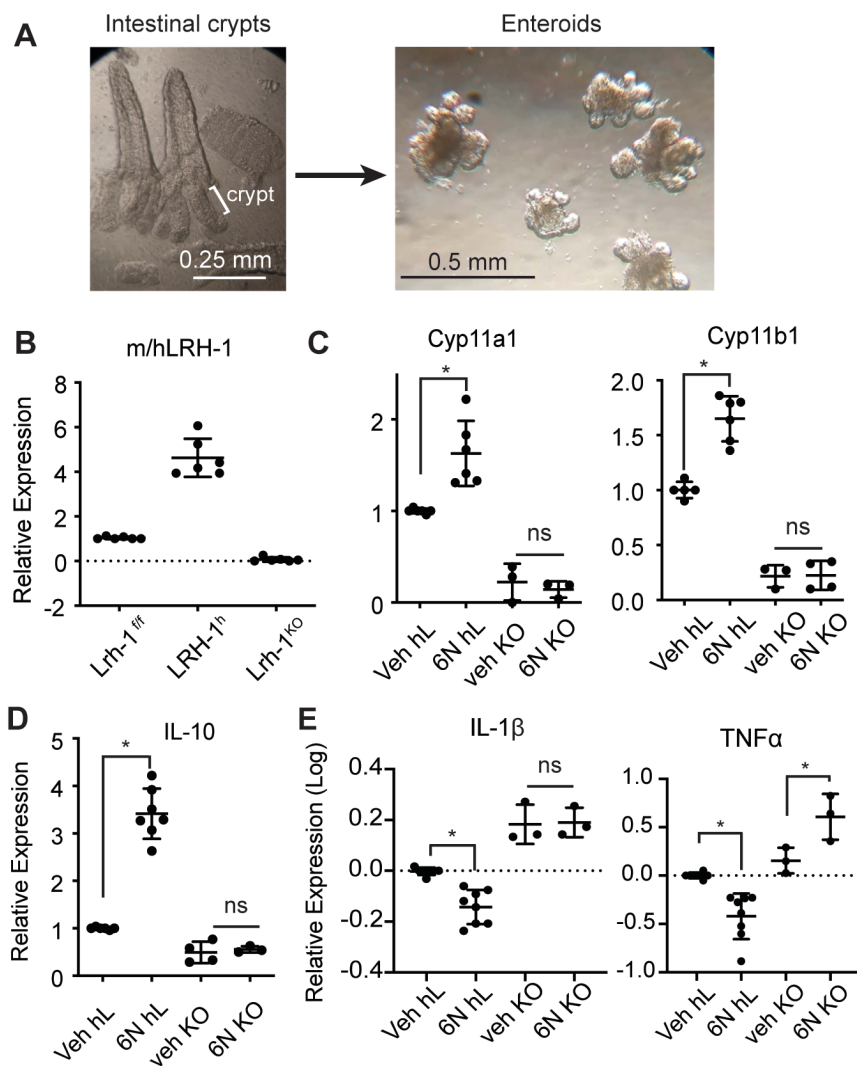
Figure 7. Compound **6N** induces intestinal epithelial steroidogenesis in humanized LRH-1 mouse enteroids. A. Enteroids were generated through isolation and culture of intestinal crypts from mice expressing human LRH-1. B. mouse or human (m/h) LRH-1 mRNA expression in the intestinal enteroids of Lrh-1[f/f], Lrh-1[KO] and LRH-1[h] mouse lines. C. Compound **6N** induces mRNA expression of steroidogenic enzyme Cyp11a1 and Cyp11b1. D. Compound **6N** induces anti-inflammatory cytokine IL-10. E. Compound **6N** reduces inflammatory cytokine IL-1β (*Left*) and TNFα (*Right*). Error bars represent the standard deviation from six biological replicates for mouse enteroids expressing human LRH-1 (hL) and three biological replicates from Lrh-1 knockout (KO) mouse enteroids. *, $p < 0.01$ (One Way ANOVA followed by Tukey's multiple comparison's test).

humanized LRH-1 mouse enteroids in the context of Tumor Necrosis Factor alpha (TNF-α)-induced inflammation. Expression of human LRH-1 in the enteroids was verified by qRT-PCR (Figure 7B). Treatment with 1 μM **6N** in hLRH-1-expressing enteroids (but not knockout enteroids) significantly increased mRNA expression of the steroidogenic enzymes Cyp11a1 and Cyp11b1, which are Lrh-1 transcriptional targets (Figure 7C). There was a concomitant increase in expression of the anti-inflammatory cytokine IL-10 and decreases in expression of the inflammatory cytokines IL-1β and TNFα (Figure 7D-E). These data suggest a role for **6N** in reducing inflammation in the gut via upregulation of steroidogenesis. These findings are in stark contrast with previous enteroid studies with RJW100, which was inactive at doses up to 20 μM[10] (dosage information not reported but obtained by personal communication with authors) Although the involvement of LRH-1 in IBD is clear from gain- and loss- of function studies[10], the finding that epithelial steroidogenesis can be stimulated by an agonist demonstrates the tremendous potential for LRH-1 as a drug target for this disease.

DISCUSSION AND CONCLUSION

While the therapeutic potential of LRH-1 is widely recognized, this receptor has been difficult to target with synthetic modulators. Agonists with the hexahydropentalene scaffold[11-12] (such as RJW100) are promising and have been used in several studies to probe LRH-1 biology[29-33]. However, we have shown that small modifications to this scaffold can greatly affect binding mode[13]. By exploiting a novel polar interaction in the LRH-1 DPP, we have overcome this challenge and have made substantial progress in agonist development. Systematic variation of three sites on the RJW100 scaffold has revealed a robust structure-activity relationship. The modifications to the styrene sites that we examined (R^2 and R^3) do not significantly improve performance and often ablate activity; however, modifications at R^1 increase potency in

transactivation assays (Figure 2C, S1). The increased potency is associated with global receptor stabilization by DSF promoted by tetrahedral, polar R^1 substituents with *endo* stereochemistry (Figure 3). In addition, the composition of the R^1 group, particularly the linker, is critical for activity. This is exemplified through the comparison of **5N** and **6N**, which differ only at the R^1 linker. Compound **6N** utilizes interactions with both Thr352 and His390 to activate LRH-1, the latter of which is likely mediated by the linker nitrogen (Figure 5D). This novel binding mode leads to a distinct mechanism of action for **6N** compared to similar, less potent compounds, inducing conformational changes at AF-B, stabilization of the AFS, and increasing coactivator association (Figure 6). Results from MDS support the idea that **6N** promotes very strong allostery to the AFS, evidenced in the strong communication between the AF-B and the AFS predicted to occur when **6N** is bound compared to less potent agonists (Figure 6).

With three separate crystal structures, we demonstrated that polar modifications at the RJW100 R^1 group do not cause major repositioning of the scaffold (Figure 5), supporting our hypothesis that this polar group acts as an important anchor point. This finding was not only key to the success of the current study, but it will also greatly benefit future work. The ability to anchor the scaffold consistently provides an opportunity to tune for additional desired effects, such as solubility or selectivity. Moreover, the trajectory of the alkyl "tails" of these molecules is amenable for introduction of modifications that could engage residues near the mouth of the pocket in a PL-like manner[18, 20]. Initial studies in this vein have been fruitful, leading to the discovery of highly active compounds[34]. Finally, the establishment of a predictable binding mode may open avenues for antagonist design; for example, by modifying the scaffold to promote displacement of the AF-H and recruitment of corepressors. This approach has been successful for other nuclear receptors[35-36] and could generate LRH-1 antagonists useful as

therapeutics for certain cancers in which LRH-1 is aberrantly active[37-43]. This is an active area of research in our laboratory.

In conclusion, a systematic, structure-guided approach has resulted in the discovery of the first low nanomolar LRH-1 agonist and elucidated a novel mechanism of action. This agonist has great potential as a tool to uncover novel aspects of LRH-1 biology and as a therapeutic for IBD and obesity-associated metabolic diseases. Equally important, the discovery of elements that stabilize the orientation of the hexahydropentalene scaffold and drive activation of LRH-1 is invaluable for understanding ligand-regulation of this receptor and for future modulator design.

EXPERIMENTAL SECTION.

General Chemical Methods. All reactions were carried out in oven-dried glassware, equipped with a stir bar and under a nitrogen atmosphere with dry solvents under anhydrous conditions, unless otherwise noted. Solvents used in anhydrous reactions were purified by passing over activated alumina and storing under argon. Yields refer to chromatographically and spectroscopically (^{1}H NMR) homogenous materials, unless otherwise stated. Reagents were purchased at the highest commercial quality and used without further purification, unless otherwise stated. n-Butyllithium (n-BuLi) was used as a 1.6 M or a 2.5 M solution in hexanes (Aldrich), was stored at 4°C and titrated prior to use. Organic solutions were concentrated under reduced pressure on a rotary evaporator using a water bath. Chromatographic purification of products was accomplished using forced-flow chromatography on 230-400 mesh silica gel. Thin-layer chromatography (TLC) was performed on 250 μm SiliCycle silica gel F-254 plates. Visualization of the developed chromatogram was performed by fluorescence quenching or by staining using KMnO4, p-anisaldehyde, or ninhydrin stains. ^{1}H and ^{13}C NMR spectra were obtained from the Emory University NMR facility and recorded on a Bruker Avance III HD 600 equipped with cryo-

probe (600 MHz), INOVA 600 (600 MHz), INOVA 500 (500 MHz), INOVA 400 (400 MHz), VNMR 400 (400 MHz), or Mercury 300 (300 MHz), and are internally referenced to residual protio solvent signals. Data for ^{1}H NMR are reported as follows: chemical shift (ppm), multiplicity (s = singlet, d = doublet, t = triplet, q = quartet, m = multiplet, dd = doublet of doublets, dt = doublet of triplets, ddd= doublet of doublet of doublets, dtd= doublet of triplet of doublets, b = broad, etc.), coupling constant (Hz), integration, and assignment, when applicable. Data for decoupled ^{13}C NMR are reported in terms of chemical shift and multiplicity when applicable. High Resolution mass spectra (HRMS) were obtained from the Emory University Mass Spectral facility. Gas Chromatography Mass Spectrometry (GC-MS) was performed on an Agilent 5977A mass spectrometer with an Agilent 7890A gas chromatography inlet. Liquid Chromatography Mass Spectrometry (LC-MS) was used to obtain low-resolution mass spectra (LRMS) and was performed on an Agilent 6120 mass spectrometer with an Agilent 1220 Infinity liquid chromatography inlet. Purity of all tested compounds was determined by HPLC analysis, using the methods given below (as indicated for each compound). All key target compounds possess >95% purity as determined by HPLC.

Method A: A linear gradient using water and 0.1 % formic acid (FA) (Solvent A) and MeCN and 0.1% FA (Solvent B); t = 0 min, 30% B, t = 4 min, 99% B (held for 1 min), then 50% B for 1 min, was employed on an Agilent Poroshell 120 EC-C18 2.7 micron, 3.0 mm x 50 mm column (flow rate 1 mL/min) or an Agilent Zorbax SB-C18 1.8 micron, 2.1 mm x 50 mm column (flow rate 0.8 mL/min). The UV detection was set to 254 nm. The LC column was maintained at ambient temperature.

Method B: A linear gradient using water and 0.1 % formic acid (FA) (Solvent A) and MeCN and 0.1% FA (Solvent B); t = 0 min, 70% B, t = 4 min, 99% B (held for 1 min), then 50% B for 1 min,

was employed on an Agilent Poroshell 120 EC-C18 2.7 micron, 3.0 mm x 50 mm column (flow

rate 1 mL/min) or an Agilent Zorbax SB-C18 1.8 micron, 2.1 mm x 50 mm column (flow rate 0.8

mL/min). The UV detection was set to 254 nm. The LC column was maintained at ambient

temperature.

Method C: An isocratic method using 75% MeCN, 35% water, and 0.1 % FA was employed on

an Agilent Poroshell 120 EC-C18 2.7 micron, 3.0 mm x 50 mm column (flow rate 1 mL/min) or

an Agilent Zorbax SB-C18 1.8 micron, 2.1 mm x 50 mm column (flow rate 0.8 mL/min). The UV

detection was set to 254 nm. The LC column was maintained at ambient temperature.

Method D: An isocratic method using 85% MeCN, 15% water, and 0.1% FA was employed on an

Agilent Poroshell 120 EC-C18 2.7 micron, 3.0 mm x 50 mm column (flow rate 1 mL/min) or an

Agilent Zorbax SB-C C18 1.8 micron, 2.1 mm x 50 mm column (flow rate 0.8 mL/min). The UV

detection was set to 254 nm. The LC column was maintained at ambient temperature.

Chemical Synthesis of 2N, 5N, and 6N. The synthesis and characterization of key target

compounds **2N**, **5N**, and **6N** are outlined below. Detailed synthetic procedures and characterization

data for all new compounds are provided in the supplemental section.

Endo   5-hexyl-4-phenyl-3a-(1-phenylvinyl)-1,2,3,3a,6,6a-hexahydropentalen-1-amine   **(1N):**

Under nitrogen, a solution of azide **S3N** (54 mg, 0.13 mmol, 1.0 equiv) in anhydrous Et_2O was

cooled to 0 °C and treated dropwise with $LiAlH_4$ (4.0M in Et_2O, 10.0 equiv). The reaction was

stirred at ambient temperature until the reaction was complete by TLC (ca. 1 h). The reaction was

cooled to 0 °C, diluted with anhydrous Et_2O, and slowly treated with water (1mL/g $LiAlH_4$).

Excess 4 M NaOH was added slowly and the solution was extracted with EtOAc three times. The

combined organic layers were washed with Rochelle's salt and brine, dried over $MgSO_4$, and

concentrated. The crude oil was purified by silica gel chromatography in 50% EtOAc/Hexanes

eluent (1% triethylamine) to afford the title compounds as a colorless oil. **1N**: 47.9 mg, 95% yield.

Purity was established by Method C: t_r = 0.302 min, 98.6%. ^{1}H NMR (600 MHz, CDCl$_3$) δ 7.37

– 7.19 (m, 10H), 5.08 (d, *J* = 1.4 Hz, 1H), 4.94 (d, *J* = 1.5 Hz, 1H), 3.30 (ddd, *J* = 11.0, 8.8, 5.7

Hz, 1H), 2.48 (d, *J* = 17.4 Hz, 1H), 2.42 (t, *J* = 9.0 Hz, 1H), 2.12 – 2.00 (m, 2H), 1.83 – 1.78 (m,

1H), 1.73 – 1.68 (m, 2H), 1.46 – 1.37 (m, 2H), 1.35 – 1.20 (m, 8H), 0.88 (t, *J* = 7.1 Hz, 3H).

N-((endo)-5-hexyl-4-phenyl-3a-(1-phenylvinyl)-1,2,3,3a,6,6a-hexahydropentalen-1-yl)acetamide

(2N) A solution of **1N** (23 mg, 0.06 mmol, 1.0 equiv) in DCM was cooled to 0 °C and treated

with acetyl chloride (1.5 equiv) and triethylamine (3.0 equiv), then stirred for 1 h. The solution

was diluted with water and extracted with DCM three times. The combined organic layers were

washed with water and brine, dried with Na$_2$SO$_4$, filtered, and concentrated. The crude oil was

purified on silica gel in 35% EtOAc/Hexanes eluent to afford the title compound as a colorless

oil. **2N**: 21.1 mg, 83% yield. Purity was established by Method D: t_R = 1.00 min, 96.3 %. ^{1}H

NMR (500 MHz, CDCl$_3$) δ 7.35 – 7.27 (m, 5H), 7.25 – 7.22 (m, 5H), 5.35 (d, *J* = 8.1 Hz, 1H),

5.06 (d, *J* = 1.5 Hz, 1H), 5.02 (d, *J* = 1.5 Hz, 1H), 4.25 (dtd, *J* = 10.5, 8.6, 6.2 Hz, 1H), 2.66

(ddd, *J* = 16.9, 8.4, 1.6 Hz, 1H), 2.14 – 2.00 (m, 4H), 1.99 (s, 3H), 1.87 (dtd, *J* = 11.7, 6.0, 2.3

Hz, 1H), 1.76 (td, *J* = 12.2, 11.7, 5.8 Hz, 1H), 1.66 (ddd, *J* = 12.7, 5.9, 2.3 Hz, 1H), 1.43 – 1.26

(m, 1H), 1.30 – 1.18 (m, 8H), 0.87 (t, *J* = 7.0 Hz, 3H). ^{13}C NMR (126 MHz, CDCl$_3$) δ 169.3,

154.6, 143.6, 141.7, 138.9, 137.2, 129.6, 127.9, 127.8, 127.7, 126.9, 126.6, 114.8, 69.0, 59.5,

54.4, 40.9, 33.0, 32.1, 31.6, 29.8, 29.4, 27.8, 26.0, 23.6, 22.6, 14.1. LRMS (ESI, APCI) *m/z*:

calc'd for C$_{30}$H$_{39}$NO [M+H]$^+$ 430.3, found 430.3

(endo)-5-hexyl-4-phenyl-3a-(1-phenylvinyl)-1,2,3,3a,6,6a-hexahydropentalen-1-yl sulfamate

(5N): A 1M solution of sulfamoyl chloride (2.5 equiv) in DMA was cooled to 0ºC. A solution of

the appropriate RJW100 alcohol isomer (*endo* (224.3 mg, 0.6 mmol 1.0 equiv) in DMA was

added slowly, followed by triethylamine (excess, ca. 5 equiv); the resulting solution was stirred

for one hour. The solution was then diluted with water and extracted with EtOAc three times.

The combined organic layers were washed with water and brine, dried with $MgSO_4$, filtered, and

concentrated. The crude oil was purified by silica gel chromatography in 20% EtOAc/Hexanes

eluent (with 0.5% triethylamine), to afford the title compound as a clear oil. **5N**: 182 mg, 67%

yield. Purity was established by Method D: t_R = 1.15 min, 95.3%. ^{1}H NMR (500 MHz, CDCl$_3$) δ

7.35 – 7.24 (m, 8H), 7.23 – 7.15 (m, 2H), 5.11 (s, 1H), 4.92 (s, 1H), 4.87 (td, J = 9.1, 5.2 Hz,

1H), 4.64 (s, 2H), 2.71 (d, J = 9.0 Hz, 1H), 2.60 (d, J = 17.5 Hz, 1H), 2.17 (dd, J = 17.7, 9.3 Hz,

1H), 2.10 – 2.01 (m, 3H), 1.92 – 1.83 (m, 1H), 1.83 – 1.76 (m, 1H), 1.68 (td, J = 12.6, 5.6 Hz,

1H), 1.45 – 1.35 (m, 2H), 1.32 – 1.16 (m, 6H), 0.86 (t, J = 7.1 Hz, 3H). ^{13}C NMR (126 MHz,

CDCl$_3$) δ 153.8, 143.5, 143.2, 138.5, 136.5, 129.8, 127.9, 127.7, 127.6, 127.0, 126.8, 115.7, 84.1,

68.2, 47.1, 34.9, 31.6, 31.2, 30.5, 29.8, 29.4, 27.7, 22.6, 14.1. LRMS (ESI, APCI) m/z: calc'd for

$C_{28}H_{36}NO_3S$ [M-H]$^-$ 465.3, found 465.4

endo 5-hexyl-4-phenyl-3a-(1-phenylvinyl)-1,2,3,3a,6,6a-hexahydropentalen-1-yl sulfamide **(6N)**

A solution of **1N** (30 mg, 0.08 mmol, 1.1 equiv) in DCM was treated with triethylamine (2.0 equiv.)

and solution of 2-oxo-1,3-oxazolidine-3-sulfonyl chloride (0.5 M in DCM, 1.0 equiv) (prepared

according to the procedure of Borghese *et al)*[44]. The reaction was stirred at room temperature for

3 h then concentrated. The residue was treated with ammonia (0.5 M in dioxane, 1.5 equiv) and

triethylamine (3.0 equiv). The solution was heated in a sealed tube at 85°C for 16 h behind a blast

shield. After cooling to ambient temperature, the reaction was diluted with 3:3:94

MeOH:Et$_3$N:EtOAc and passed through a pad of silica. The eluent was concentrated, and the crude

oil was purified on silica in 20-30% EtOAc/hexanes eluent to afford the title compound as a

colorless oil. **6N**: 21.6 mg, 60% yield. Purity was established by Method C: t_R = 2.0 min, 96.6 %.

^{1}H NMR (600 MHz, CDCl$_3$) δ 7.33 – 7.23 (m, 8H), 7.20 – 7.17 (m, 2H), 5.09 (d, J = 1.3 Hz, 1H), 4.96 (d, J = 1.3 Hz, 1H), 4.44 (s, 2H), 4.36 (d, J = 8.0 Hz, 1H), 3.84 – 3.77 (m, 1H), 2.62 (td, J = 8.9, 2.0 Hz, 1H), 2.38 (dd, J = 17.5, 2.0 Hz, 1H), 2.20 – 2.13 (m, 1H), 2.08 – 2.04 (m, 2H), 2.00 – 1.95 (m, 1H), 1.74 – 1.70 (m, 2H), 1.50 – 1.43 (m, 1H), 1.42 – 1.16 (m, 8H), 0.86 (t, J = 7.1 Hz, 3H). ^{13}C NMR (126 MHz, CDCl$_3$) δ 154.1, 143.6, 142.8, 139.3, 136.6, 129.6, 127.8, 127.7, 126.9, 126.8, 115.5, 68.8, 57.2, 47.4, 35.4, 32.3, 32.0, 31.6, 29.8, 29.5, 27.9, 22.6, 14.1. LRMS (ESI, APCI) *m/z*: calc'd for C$_{28}$H$_{37}$N$_2$O$_2$S [M+H]$^+$ 465.7, found 464.8

Biology: materials and reagents. pCI empty vector was purchased from Promega. The SHP-luc and *Renilla* reporters, as well as pCI LRH-1, have been previously described[18]. The vector for His-tagged tobacco etch virus (TEV) was a gift from John Tesmer (University of Texas at Austin). The pMSC7 (LIC-HIS) vector was provided by John Sondek (University of North Carolina at Chapel Hill). The Tif2 NR Box 3 peptide was purchased from RS Synthesis. DNA oligonucleotide primers were synthesized by Integrated DNA Technologies.

Protein purification. Purification of human LRH-1 ligand binding domain (residues 300-537) in a pMCSG7 expression vector was performed as described[13]. Briefly, protein was expressed in BL21 PLysS *E. coli*, using 1 mM IPTG for 4 hours (30°C) to induce expression. Protein was purified by nickel affinity chromatography. For DSF assays, protein eluted from the nickel column was exchanged with DLPC (5-fold molar excess overnight at 4 °C), followed by repurification by size exclusion to remove displaced lipids. The assay buffer was 20 mM Tris-HCl, pH 7.5, 150 mM sodium chloride, and 5% glycerol. Cleaved LRH-1 was then incubated with ligands overnight at 4 °C prior to repurification by size exclusion, using the same assay buffer as for DSF. Protein used for crystallography was prepared as for coregulator recruitment, except that it was sized into

a buffer of 100 mM ammonium acetate (pH 7.5), 150 mM sodium chloride, 1 mM DTT, 1 mM EDTA, and 2 mM CHAPS.

Differential scanning fluorimetry (DSF). DSF assays were conducted on a StepOne Plus thermocycler as previously described[13, 15]. Briefly, aliquots of purified LRH-1 LBD protein (0.2 mg/ ml) were incubated with saturating concentrations of ligand overnight at 4 °C. Protein-ligand complexes were heated in the presence of SYPRO orange dye at a rate of 0.5 degree/ minute. Complexes were excited at 488 nm, and fluorescence emissions at each degree Celsius were measured using the ROX filter (~600 nm). Tm values were calculated using the Bolzmann equation in GraphPad Prism, v7.

Crystallography. Compounds **5N**, **6N***, or **2N** were incubated with purified LRH-1 LBD (His tag removed) at 5-fold molar excess overnight at 4°C. The complexes were re-purified by size exclusion chromatography into the crystallization buffer (see above). Protein was concentrated to 5-6 mg/ ml and combined with a peptide from human Tif2 NR box 3 (H3N-KENALLRYLLDKDDT-CO2) at four-fold molar excess. Crystals were generated by hanging drop vapor diffusion at 18 °C, using a crystallant of 0.05 M sodium acetate (pH 4.6), 5-11% PEG 4000, and 0-10% glycerol. Crystals of **2N** with LRH-1 were generated by microseeding, using RJW100-LRH-1 crystals as the seed stocks (crystals used for seeding were grown as described)[13].

Structure Determination. Crystals were flash-frozen in liquid nitrogen, using a cryoprotectant of crystallant plus 30% glycerol. Diffraction data were collected remotely from Argonne National Laboratory, Southeast Regional Collaborative Access Team, Beamline 22ID. Data were processed and scaled using HKL2000[45]. Structures were phased by molecular replacement using Phenix[46], with PBD 5L11 used as the search model. The structure was refined using phenix.refine[46] and Coot[47], with some additional refinement done using the PDB Redo web server[48].

Tissue culture. Hela cells were purchased from Atlantic Type Culture Collection and cultured in phenol red-free MEMα media supplemented with 10% charcoal-dextran-stripped fetal bovine serum. Cells were maintained under standard culture conditions.

Reporter gene assays. Hela cells were reverse-transfected with three vectors: (1) full-length, human LRH-1 in a pCI vector, (2) a firefly reporter (pGL3 Basic) with a portion of the SHP promoter cloned upstream of the firefly luciferase gene, and (3) a constitutively active vector expressing *Renilla* luciferase under control of the CMV promoter. To study SF-1 activity, cells were transfected with the same constructs, except that full-length SF-1 (in a pcDNA3.1 vector) was overexpressed instead of LRH-1, with empty pcDNA3.1 used as the negative control. Transfections utilized the Fugene HD transfection reagent at a ratio of 5 μl per 2 μg DNA. To perform the reverse transfections, cells were trypsinized, combined with the transfection mixture, and plated at densities of 7,500 cells per well in white-walled 96-well plates. The following day, cells were treated with each compound (or DMSO control) for 24 hours. In most cases, six points in the concentration range of $0.03 - 30$ μM were used (exceptions noted in figures), with a final DMSO concentration of 0.3% in all wells. Luciferase expression was measured using the DualGlo Kit (Promega). Firefly luciferase signal was normalized to *Renilla* luciferase signal in each well. EC_{50} values were calculated using three-parameter curve-fitting (GraphPad Prism, v.7). Assays were conducted in triplicate with at least two independent biological replicates. Experiments involving SF-1 activation were conducted in an identical manner, except full-length human SF-1 (in a pcDNA3.1+ vector) was overexpressed instead of LRH-1. Significance of differences in luminescence signal for LRH-1 *versus* SF-1 promoted by particular agonists was determined using two-way ANOVA followed by Sidak's multiple comparisons test.

Calculation of Relative Efficacy (RE). This value was calculated from curve-fitting to data from luciferase reporter assays. To compare the maximum activities of the new compounds to RJW100, we used the formula $(Max_{cpd} - Min_{cpd}) / (Max_{RJW100} - Min_{RJW100})$, where "Max" and "Min" denote the dose response curve maximum and minimum, respectively. A RE of 0 indicates a completely inactive compound, a value of 1 indicates equal activity to RJW100, and values above 1 indicate greater activity.

Mutagenesis. Mutations were introduced to LRH-1 in the pCI vector using the Quikchange Lightning site-directed mutagenesis kit (Ambion). Constructs were sequenced prior to use in reporter gene assays as described above.

Model Construction for Molecular Dynamics Simulations. Four LRH-1 LBD complexes were prepared for molecular dynamics simulations. 1) LRH-1-Tif2-RJW100 (PDB 5L11), 2) LRH-1-Tif2-**5N**. 3LRH-1-Tif2-**2N**, LRH-1-Tif2-**6N**. For consistency, all structures contained LRH-1 residues 300–540. Missing residues (i.e., that could not be modeled in the structures) were added to the models used in the simulations.

Molecular Dynamics Simulations. The complexes were solvated in an octahedral box of TIP3P water with a 10-Å buffer around the protein complex. Na^+ and Cl^- ions were added to neutralize the protein and achieve physiological buffer conditions. All systems were set up using the xleap tool in AmberTools17[49] with the ff14SB forcefield[50]. Parameters for the agonist ligands **6N**, **2N** and **5N** were obtained using Antechamber[51] also in AmberTools17. All minimizations and simulations were performed with Amber16[49]. Systems were minimized with 5000 steps of steepest decent followed by 5000 steps of conjugate gradient minimization with 500-kcal/mol·$Å^2$ restraints on all solute atoms. Restraints were removed excluding the atoms in both the ligand and the Tif2 peptide, and the previous minimization was repeated. This minimization was repeated with

restraints lowered to 100- kcal/mol·$Å^2$. Finally, all restraints were removed for a last minimization step. The systems were heated from 0 to 300 K using a 100-ps run with constant volume periodic boundaries and 5-kcal/mol·$Å^2$ restraints on all protein and ligand atoms. MD equilibration was performed for 12 ns with 10-kcal/mol·$Å^2$ restraints on Tif2 peptide and ligand atoms using the NPT ensemble. Restraints were reduced to 1 kcal/mol·$Å^2$ for an additional 10 ns of MD equilibration. Then, restraints were removed, and 1000-ns production simulations were performed for each system in the NPT ensemble. A 2-fs time step was used with all bonds between heavy atoms and hydrogens fixed with the SHAKE algorithm[52]. A cutoff distance of 10 Å was used to evaluate long-range electrostatics with particle mesh Ewald and for van der Waals forces. Fifty thousand evenly spaced frames were taken from each simulation for analysis, using the CPPTRAJ module[53] of AmberTools. The NetworkView plugin[21] in VMD[54] and the Carma program[55] were used to produce dynamic networks for each system. In brief, networks are constructed by defining all protein C-α atoms as nodes, using Cartesian covariance to measure communication within the network. Pairs of nodes that reside within a 4.5-Å cutoff for 75% of the simulation are connected via an edge. Edge weights are inversely proportional to the covariance between the nodes. Networks were constructed using 500 ns of the MDS trajectories, to enable direct comparison with our previous LRH-1-RJW MDS[15]. Suboptimal paths between the AF-B and Tif2 peptide were identified using the Floyd-Warshall algorithm[56]. Suboptimal path analyses were performed using Carma and the subopt program in NetworkView. Cross-correlation matrices for C-α atoms in each system were computed with Carma.

Coregulator Recruitment Assays. Synthetic agonists were titrated in the presence of purified LRH-1 LBD protein (2 μM) and a fluorescein (FAM)-labeled peptide corresponding to the Tif2 NR box 3 (FAM-H_3N-PVSPKKKENALLRYLLDKDDT-CO_2^-) (50 nM). Protein and probe

concentrations were determined from preliminary experiments titrating LRH-1 protein with no ligand added in the presence of FAM-Tif2 (2 µM was slightly above the Tif2 Kd in these experiments). Tif2 binding was detected by fluorescence polarization, using a BioTek Neo plate reader. Assays were conducted three times in triplicate, using two separate protein preparations. Significance of differences in Tif2 association at each dose was determined using two-way ANOVA followed by Tukey's multiple comparisons test.

Hydrogen-deuterium exchange mass spectrometry. Following cleavage of the His tag from purified LRH-1 LBD with TEV protease as described above, the protein was further purified by size exclusion chromatography into a buffer of phosphate buffered saline (pH 7.5) plus 5% glycerol. Protein purity exceeded 98% by Coomassie staining. Protein-ligand complexes were prepared by adding each ligand at 5-fold molar excess to 2 mg/ml protein and incubating overnight at 4 °C. Complexes were centrifuged to remove any aggregates prior to analysis by HDX-MS. HDX-MS was conducted using Waters' UPLC HDX system coupled with a Q-Tof Premier mass spectrometer (Waters Corp, Milford, MA). Protein-ligand complexes were diluted 1:7 (v/v) into labeling buffer (protein buffer containing D_2O instead of water) via an autosampler. Labeling took place at 20°C for time periods of 0, 10, 100, 1,000, and 10,000 seconds prior to quenching in with equal volume of precooled quenching buffer (100 mM phosphate, 0.5 M tris)2-carboxyethl)phosphine, 0.8% formic acid, and 2% acetonitrile, pH 2.5, 1°C). After quenching, samples were applied to a Waters enzymate pepsin column (2.1 x 30 mm). Peptides from the pepsin column were separated in-line on a Waters Acuity UPLC BEH C18 column (1.7 µM, 1.0 x 100 mm) at a flow of 40 µl/ min for 12 minutes (8-40% linear gradient, mobile phase: 0.1% formic acid in acetonitrile) at 1°C. The mass spectrometer was operated with the electrospray ionization source in positive ion mode, and the data were acquired in elevated-energy mass spectrometry

mode. For internal calibration, a reference lock-mass of Glu-Fibrinopeptide (Sigma-Aldrich, St Louis, MO) was acquired along with each sample data collection. Peptides were identified by comparison to human LRH-1 protein sequence using the ProteinLynx Global SERVER (version 3.02). HDX data were processed in DynamX (version 3.0). Mass assignment for each peptide at 0 seconds of exchange was checked manually, and any assignment with a mass deviation > 0.2 Da was removed. Hydrogen-deuterium exchange protection was quantified by comparison of hydrogen exchange profiles at different time points. Peptide coverage was 99.2% for this experiment (Figure S4).

Humanized LRH-1 mouse intestinal enteroid culture. The study protocol was approved by the Animal Care and Use Committee of Baylor College of Medicine and was in accordance with the Guide for the Care and Use of Laboratory Animals [DHHS publication no. (NIH) 85-23, revised 1985, Office of Science and Health Reports, DRR/NIH, Bethesda, MD 20205].

The humanized LRH-1 allele (LRH-1^h) is obtained on a mouse line with a human LRH-1 transgene using the Rosa26-loxP-STOP-loxP strategy to allow villin-cre mediated expression of human LRH-1 (LRH-1$^{\Delta\Delta}$) in enterocytes with knockout of the endogenous mLrh-1 (Lrh-1$^{f/f}$). Intestinal crypt culture (enteroids) were derived from Lrh1$^{f/f}$, Lrh-1^{KO} (Lrh1$^{f/f}$;Villin-Cre$^+$), and LRH-1^h (Lrh1$^{f/f}$;hLRH1$^{\Delta\Delta}$;Villin-Cre$^+$) male mice (6-8 weeks old). Briefly, the small intestine was isolated and flushed with ice-cold phosphate-buffered saline (PBS), opened longitudinally, then cut into 1–2 mm pieces. Intestinal fragments were incubated in an EDTA (4 mM) containing solution at 4 °C for 60 min on a tube rocker. The intestinal fragment suspension was fractionated by vertical shaking manually and crypt-containing fractions passed through a 70-μm cell strainer for plating in Matrigel. Crypt-Matrigel suspension was allowed to polymerize at 37 °C for 15 min. Intestinal

organoids were grown in base culture media (Advanced DMEM/F12 media, HEPES, GlutaMax, penicillin, and streptomycin) supplemented with growth factors (EGF, Noggin, R-spondin, R&D Systems), B27 (Life Technologies), N2 (Life Technologies), and N-acetyl cysteine (NAC, Sigma). Intestinal enteroids were passaged every 3 days. Established LRH-1^h enteroids were treated with mouse TNF-   overnight to provoke inflammatory changes, then treated with vehicle (DMSO) or compound 6N (1   M) overnight. Following treatment, enteroid tissues were harvested for real time PCR.

RNA isolation and PCR. Intestinal enteroids were washed in ice-cold PBS and suspended in Trizol solution (Sigma). RNA was isolated with RNeasy® spin columns (Qiagen). DNAse-treated total RNA was used to generate cDNA using Superscript II (Quanta). Sybr green-based qPCR (Kapa Biosystems) was performed on a Roche LightCycler® 480 II with primers as shown below. The ΔΔCt method was used for calculating gene expression fold changes using Rplp0 (ribosomal protein, large, P0, known as 36B4) as reference. Primer sequences were as follows:

Gene	Forward (5'→3')	Reverse (5'→3')
m/hLRH-1*	GTGTCTCAAT TTAAAATGGT GAATTACTCC TATGATGAAG ATCTGGAAGAGCT	AAT AAGTTTGGGC CAATGTACAA GAGAGACAGG GC
Cyp11a1	GCTGGAAGGTGTAGCTCAGG	CACTGGTGTGGAACATCTGG
Cyp11b1	Primers purchased from QuantiTect®, Qiagen (NM_001033229, catalog # QT01198575)	
IL-10	GCCTTATCGGAAATGATCCAGT	GCTCCACTGCCTTGCTCTTATT
IL-1β	Primers purchased from QuantiTect®, Qiagen (NM_008361, catalog # QT01048355)	
TNFα	CCAGAAAAGACACCATGAGCAC	GGGCCATAGAACTGATGAGAGG
Rplp0(36B4)	GAAACTGCTGCCTCACATCCG	GCTGGCACAGTGACCTCACAC

* This set of primers are designed to amplify both mouse and human (m/h) LRH-1 cDNA.

ASSOCIATED CONTENT

AUTHOR INFORMATION

Corresponding Author

*Eric A. Ortlund

1525 Clifton Rd. G235

Atlanta, GA 30322

eortlun@emory.edu

Present Addresses

Author Contributions

All authors contributed to this manuscript and approve the final version.

ABBREVIATIONS

LRH-1, Liver Receptor Homolog-1; DLPC, dilauroylphosphatidylcholine; DPP, deep polar

portion of the LRH-1 binding pocket; DSF, differential scanning fluorimetry; RE, relative

efficacy; i.a., inactive; PL, phospholipid; Tif2, transcriptional intermediary factor 2; AFS,

activation function surface; AF-H, activation function helix; SF-1, steroidogenic factor-1; LBD,

ligand binding domain; HDX, hydrogen-deuterium exchange; AF-B, helix 6/β sheet; MDS,

molecular dynamics simulation; qRT-PCR, quantitative real time polymerase chain reaction;

veh, vehicle; h, hour; NR, nuclear receptor; DMSO, dimethylsulfoxide; Cyp11a1, Cytochrome

P450 family 11 subfamily a member 1; Cyp11b1, Cytochrome P450 family 11 subfamily b

member 1; IL-10, Interleukin 10; IL-1 , Interleukin 1-beta; IBD, inflammatory bowel disease.

PDB CODES
Authors will release the atomic coordinates and experimental data upon article publication. PDB

IDs have been provided in figure legends and are as follows: LRH-1-**5N**, 6OQX; LRH-1-**6N**,

6OQY; LRH-1-**2N**, 6OR1.

SUPPORTING INFORMATION AVAILABILITY

The Supporting Information is available free of charge on the ACS Publications website:

- Dose-response curves for all luciferase reporter assay experiments (Figure S1).
- HDX peptide coverage and deuterium uptake plots (Figure S2).
- X-ray data collection and refinement statistics (Table S1).
- Synthetic procedures, NMR, MS, HPLC (purity), and MS data for all compounds synthesized. ^{1}H, ^{13}C NMR spectra of **2N, 5N, 6N** (PDF)
- Molecular Formula Strings (CSV)

REFERENCES

1.   Gu, P.; Goodwin, B.; Chung, A. C.; Xu, X.; Wheeler, D. A.; Price, R. R.; Galardi, C.; Peng, L.; Latour, A. M.; Koller, B. H.; Gossen, J.; Kliewer, S. A.; Cooney, A. J., Orphan Nuclear Receptor Lrh-1 Is Required to Maintain Oct4 Expression at the Epiblast Stage of Embryonic Development. *Molecular and cellular biology* **2005,** *25* (9), 3492-3505.

2.   Nissim, S.; Weeks, O.; Talbot, J. C.; Hedgepeth, J. W.; Wucherpfennig, J.; Schatzman-Bone, S.; Swinburne, I.; Cortes, M.; Alexa, K.; Megason, S.; North, T. E.; Amacher, S. L.; Goessling, W., Iterative Use of Nuclear Receptor Nr5a2 Regulates Multiple Stages of Liver and Pancreas Development. *Dev Biol* **2016,** *418* (1), 108-123.

3.   Lu, T.; Makishima, M.; JJ, R.; Schoonjans, K.; Kerr, T.; Auwerx, J.; DJ, M., Molecular Basis for Feedback Regulation of Bile Acid Synthesis by Nuclear Receptors. *Molecular Cell* **2000,** *6*, 507-515.

4.   Schoonjans, K.; Annicotte, J.-S.; Huby, T.; Botrugno, O.; Fayard, E.; Ueda, Y.; Chapman, J.; Auwerx, J., Liver Receptor Homolog 1 Controls the Expression of the Scavenger Receptor Class B Type I. *EMBO Reports* **2002,** *3* (12), 1181-1187.

5.   Stein, S.; Oosterveer, M. H.; Mataki, C.; Xu, P.; Lemos, V.; Havinga, R.; Dittner, C.; Ryu, D.; Menzies, K. J.; Wang, X.; Perino, A.; Houten, S. M.; Melchior, F.; Schoonjans, K., Sumoylation-Dependent Lrh-1/Prox1 Interaction Promotes Atherosclerosis by Decreasing Hepatic Reverse Cholesterol Transport. *Cell metabolism* **2014,** *20* (4), 603-613.

6.   Lee, J. M.; Lee, Y. K.; Mamrosh, J. L.; Busby, S. A.; Griffin, P. R.; Pathak, M. C.; Ortlund, E. A.; Moore, D. D., A Nuclear-Receptor-Dependent Phosphatidylcholine Pathway with Antidiabetic Effects. *Nature* **2011,** *474* (7352), 506-510.

7.   Stein, S., Lemos, V. Xu, P., Demagny, H., Wang, X., Ryu, D., Jimenez, V., Bosch, F., Luscher, T.F., Oosterveer M.H., Schoonjans, K., Impaired Sumoylation of Nuclear Receptor Lrh-1 Promotes Nonalcoholic Fatty Liver Disease. *The Journal of clinical investigation* **2016,** *127* (2), 583-592.

8.   Bolado-Carrancio, A.; Riancho, J. A.; Sainz, J.; Rodriguez-Rey, J. C., Activation of Nuclear Receptor Nr5a2 Increases Glut4 Expression and Glucose Metabolism in Muscle Cells. *Biochemical and biophysical research communications* **2014,** *446* (2), 614-619.

9.   Oosterveer, M. H.; Mataki, C.; Yamamoto, H.; Harach, T.; Moullan, N.; van Dijk, T. H.; Ayuso, E.; Bosch, F.; Postic, C.; Groen, A. K.; Auwerx, J.; Schoonjans, K., Lrh-1-Dependent Glucose Sensing Determines Intermediary Metabolism in Liver. *The Journal of clinical investigation* **2012,** *122* (8), 2817-2826.

10.   Bayrer, J. R.; Wang, H.; Nattiv, R.; Suzawa, M.; Escusa, H. S.; Fletterick, R. J.; Klein, O. D.; Moore, D. D.; Ingraham, H. A., Lrh-1 Mitigates Intestinal Inflammatory Disease by Maintaining Epithelial Homeostasis and Cell Survival. *Nature communications* **2018,** *9* (1), 4055.

11.   Whitby, R. J.; Dixon, S.; Maloney, P. R.; Delerive, P.; Goodwin, B.; Parks, D. J.; Wilson, T. M., Identification of Small Molecule Agonists of the Orphan Nuclear Receptros Liver Receeoptor Homolog-1 and Steroidogenic Factor-1. *Journal of medicinal chemistry* **2006,** *49*, 6652-6655.

12.   Whitby, R. J.; Stec, J.; Blind, R. D.; Dixon, S.; Leesnitzer, L. M.; Orband-Miller, L. A.; Williams, S. P.; Willson, T. M.; Xu, R.; Zuercher, W. J.; Cai, F.; Ingraham, H. A., Small Molecule Agonists of the Orphan Nuclear Receptors Steroidogenic Factor-1 (Sf-1, Nr5a1) and Liver Receptor Homologue-1 (Lrh-1, Nr5a2). *Journal of medicinal chemistry* **2011,** *54* (7), 2266-2281.

13.   Mays, S. G.; Okafor, C. D.; Whitby, R. J.; Goswami, D.; Stec, J.; Flynn, A. R.; Dugan, M. C.; Jui, N. T.; Griffin, P. R.; Ortlund, E. A., Crystal Structures of the Nuclear Receptor, Liver Receptor Homolog 1, Bound to Synthetic Agonists. *The Journal of biological chemistry* **2016,** *291* (49), 25281-25291.

14.   Thomas, E., Dixon, S. Whitby, R.J., A Rearrangement to a Zirconium-Alkenylidene in the Insertion of Dihalocarvvenoids and Acetylides into Ziconacycles. *Angew Chemie Int* **2006,** *45* (43), 7070-7072.

15.   Mays, S. G.; Okafor, C. D.; Tuntland, M. L.; Whitby, R. J.; Dharmarajan, V.; Stec, J.; Griffin, P. R.; Ortlund, E. A., Structure and Dynamics of the Liver Receptor Homolog 1-Pgc1alpha Complex. *Molecular pharmacology* **2017,** *92* (1), 1-11.

16.   Burnley, B. T.; Afonine, P. V.; Adams, P. D.; Gros, P., Modelling Dynamics in Protein Crystal Structures by Ensemble Refinement. *eLife* **2012,** *1*, e00311.

17.   Ortlund, E. A.; Lee, Y.; Solomon, I. H.; Hager, J. M.; Safi, R.; Choi, Y.; Guan, Z.; Tripathy, A.; Raetz, C. R.; McDonnell, D. P.; Moore, D. D.; Redinbo, M. R., Modulation of Human Nuclear Receptor Lrh-1 Activity by Phospholipids and Shp. *Nature structural & molecular biology* **2005,** *12* (4), 357-363.

18.   Musille, P. M.; Pathak, M. C.; Lauer, J. L.; Hudson, W. H.; Griffin, P. R.; Ortlund, E. A., Antidiabetic Phospholipid-Nuclear Receptor Complex Reveals the Mechanism for Phospholipid-Driven Gene Regulation. *Nature structural & molecular biology* **2012,** *19* (5), 532-537, S531-532.

19.   Musille, P. M.; Kossmann, B. R.; Kohn, J. A.; Ivanov, I.; Ortlund, E. A., Unexpected Allosteric Network Contributes to Lrh-1 Coregulator Selectivity. *The Journal of biological chemistry* **2015,** *291* (3), 1411-1426.

20.   Sablin, E. P.; Blind, R. D.; Uthayaruban, R.; Chiu, H. J.; Deacon, A. M.; Das, D.; Ingraham, H. A.; Fletterick, R. J., Structure of Liver Receptor Homolog-1 (Nr5a2) with Pip Hormone Bound in the Ligand Binding Pocket. *Journal of structural biology* **2015,** *192*, 342-348.

21.   Sethi, A.; Eargle, J.; Black, A. A.; Luthey-Schulten, Z., Dynamical Networks in Trna:Protein Complexes. *Proceedings of the National Academy of Sciences of the United States of America* **2009,** *106* (16), 6620-6625.

22.   Gasper, P. M.; Fuglestad, B.; Komives, E. A.; Markwick, P. R. L.; McCammon, J. A., Allosteric Networks in Thrombin Distinguish Procoagulant Vs. Anticoagulant Activities. *Proceedings of the National Academy of Sciences* **2012,** *109* (52), 21216-21222.

23.   VanWart, A. T.; Eargle, J.; Luthey-Schulten, Z.; Amaro, R. E., Exploring Residue Component Contributions to Dynamical Network Models of Allostery. *Journal of Chemical Theory and Computation* **2012,** *8* (8), 2949-2961.

24.   Bowerman, S.; Wereszczynski, J., Detecting Allosteric Networks Using Molecular Dynamics Simulation. *Methods in enzymology* **2016,** *578*, 429-447.

25.   Van Wart, A. T.; Durrant, J.; Votapka, L.; Amaro, R. E., Weighted Implementation of Suboptimal Paths (Wisp): An Optimized Algorithm and Tool for Dynamical Network Analysis. *Journal of Chemical Theory and Computation* **2014,** *10* (2), 511-517.

26.   Mueller, M.; Cima, I.; Noti, M.; Fuhrer, A.; Jakob, S.; Dubuquoy, L.; Schoonjans, K.; Brunner, T., The Nuclear Receptor Lrh-1 Critically Regulates Extra-Adrenal Glucocorticoid Synthesis in the Intestine. *J Exp Med* **2006,** *203* (9), 2057-2062.

27.   Fernandez-Marcos, P. J.; Auwerx, J.; Schoonjans, K., Emerging Actions of the Nuclear Receptor Lrh-1 in the Gut. *Biochim Biophys Acta* **2011,** *1812* (8), 947-955.

28.   Basak, O.; Beumer, J.; Wiebrands, K.; Seno, H.; van Oudenaarden, A.; Clevers, H., Induced Quiescence of Lgr5+ Stem Cells in Intestinal Organoids Enables Differentiation of Hormone-Producing Enteroendocrine Cells. *Cell Stem Cell* **2017,** *20* (2), 177-190 e174.

29. Zhang, Y.; Yang, Z.; Whitby, R.; Wang, L., Regulation of Mir-200c by Nuclear Receptors Pparalpha, Lrh-1 and Shp. *Biochemical and biophysical research communications* **2011,** *416* (1-2), 135-139.

30. Mamrosh, J. L.; Lee, J. M.; Wagner, M.; Stambrook, P. J.; Whitby, R. J.; Sifers, R. N.; Wu, S. P.; Tsai, M. J.; Demayo, F. J.; Moore, D. D., Nuclear Receptor Lrh-1/Nr5a2 Is Required and Targetable for Liver Endoplasmic Reticulum Stress Resolution. *eLife* **2014,** *3*, e01694.

31. Cobo-Vuilleumier, N.; Lorenzo, P. I.; Rodriguez, N. G.; Herrera Gomez, I. G.; Fuente-Martin, E.; Lopez-Noriega, L.; Mellado-Gil, J. M.; Romero-Zerbo, S. Y.; Baquie, M.; Lachaud, C. C.; Stifter, K.; Perdomo, G.; Bugliani, M.; De Tata, V.; Bosco, D.; Parnaud, G.; Pozo, D.; Hmadcha, A.; Florido, J. P.; Toscano, M. G.; de Haan, P.; Schoonjans, K.; Sanchez Palazon, L.; Marchetti, P.; Schirmbeck, R.; Martin-Montalvo, A.; Meda, P.; Soria, B.; Bermudez-Silva, F. J.; St-Onge, L.; Gauthier, B. R., Lrh-1 Agonism Favours an Immune-Islet Dialogue Which Protects against Diabetes Mellitus. *Nature communications* **2018,** *9* (1), 1488.

32. Venteclef, N.; Jakobsson, T.; Ehrlund, A.; Damdimopoulos, A.; Mikkonen, L.; Ellis, E.; Nilsson, L. M.; Parini, P.; Janne, O. A.; Gustafsson, J. A.; Steffensen, K. R.; Treuter, E., Gps2-Dependent Corepressor/Sumo Pathways Govern Anti-Inflammatory Actions of Lrh-1 and Lxrbeta in the Hepatic Acute Phase Response. *Genes & development* **2010,** *24* (4), 381-395.

33. Lee, J. S.; Bae, S.; Kang, H. S.; Im, S. S.; Moon, Y. A., Liver Receptor Homolog-1 Regulates Mouse Superoxide Dismutase 2. *Biochemical and biophysical research communications* **2017,** *489* (3), 299-304.

34. Flynn, A. R.; Mays, S. G.; Ortlund, E. A.; Jui, N. T., Development of Hybrid Phospholipid Mimics as Effective Agonists for Liver Receptor Homologue-1. *ACS Medicinal Chemistry Letters* **2018,** *9* (10), 1051-1056.

35. Shiau, A. K., Barstad, D., Loria, P.M., Cheng, L., Kushner, P.J., Agard, D.A., Greene, G.L., The Structural Basis of Estrogen Receptor/ Coactivator Recognition and the Antagonism of This Interaction by Tamoxifen. *Cell* **1998,** *95* (7), 927-937.

36. Raaijmakers, H. C.; Versteegh, J. E.; Uitdehaag, J. C., The X-Ray Structure of Ru486 Bound to the Progesterone Receptor in a Destabilized Agonistic Conformation. *The Journal of biological chemistry* **2009,** *284* (29), 19572-19579.

37. Thiruchelvam, P. T.; Lai, C. F.; Hua, H.; Thomas, R. S.; Hurtado, A.; Hudson, W.; Bayly, A. R.; Kyle, F. J.; Periyasamy, M.; Photiou, A.; Spivey, A. C.; Ortlund, E. A.; Whitby, R. J.; Carroll, J. S.; Coombes, R. C.; Buluwela, L.; Ali, S., The Liver Receptor Homolog-1 Regulates Estrogen Receptor Expression in Breast Cancer Cells. *Breast cancer research and treatment* **2011,** *127* (2), 385-396.

38. Safi, R., Kovacic, A., Gaillard, S., Murata, Y., Simpson, E.R., McDonnell, D.P., Clyne, C.D., Coactivation of Liver Receptor Homologues-1 by Peroxisome Proliferator-Activated Receptor Gamma Coactivator-1 Alpha on Aromatase Promoter Ii and Its Inhibition by Activated Retinoid X Receptor Suggest a Novel Target for Breast-Specific Antiestrogen Therapy. *Cancer research* **2005,** *65* (24), 11762-11770.

39. Nadolny, C.; Dong, X., Liver Receptor Homolog-1 (Lrh-1): A Potential Therapeutic Target for Cancer. *Cancer Biol Ther* **2015,** *16* (7), 997-1004.

40. Lin, Q.; Aihara, A.; Chung, W.; Li, Y.; Huang, Z.; Chen, X.; Weng, S.; Carlson, R. I.; Wands, J. R.; Dong, X., Lrh1 as a Driving Factor in Pancreatic Cancer Growth. *Cancer letters* **2014,** *345* (1), 85-90.

41.   Chand, A. L.; Herridge, K. A.; Thompson, E. W.; Clyne, C. D., The Orphan Nuclear Receptor Lrh-1 Promotes Breast Cancer Motility and Invasion. *Endocrine-related cancer* **2010,** *17* (4), 965-975.

42.   Lai, C. F.; Flach, K. D.; Alexi, X.; Fox, S. P.; Ottaviani, S.; Thiruchelvam, P. T.; Kyle, F. J.; Thomas, R. S.; Launchbury, R.; Hua, H.; Callaghan, H. B.; Carroll, J. S.; Charles Coombes, R.; Zwart, W.; Buluwela, L.; Ali, S., Co-Regulated Gene Expression by Oestrogen Receptor Alpha and Liver Receptor Homolog-1 Is a Feature of the Oestrogen Response in Breast Cancer Cells. *Nucleic acids research* **2013,** *41* (22), 10228-10240.

43.   Bayrer, J. R.; Mukkamala, S.; Sablin, E. P.; Webb, P.; Fletterick, R. J., Silencing Lrh-1 in Colon Cancer Cell Lines Impairs Proliferation and Alters Gene Expression Programs. *Proceedings of the National Academy of Sciences of the United States of America* **2015,** *112* (8), 2467-2472.

44.   Borghese, A., Antoine, L., Van Hoeck, J.P., Merschaert, A. , Mild and Safer Perparative Method for Nonsymmetrical Sulfamides Via *N*-Sulfamyloxazolidinone Derivatives: Electronic Effects Affect the Trassulfamoylation Reactivity. *Org Process Res Dev* **2006,** *10* (4), 770-775.

45.   Otwinowski, Z., Minor, W., Processing of X-Ray Diffraction Data Collected in Oscillation Mode. *Methods in Enzymology* **1997,** *276*, 307-326.

46.   Adams, P. D.; Afonine, P. V.; Bunkoczi, G.; Chen, V. B.; Davis, I. W.; Echols, N.; Headd, J. J.; Hung, L. W.; Kapral, G. J.; Grosse-Kunstleve, R. W.; McCoy, A. J.; Moriarty, N. W.; Oeffner, R.; Read, R. J.; Richardson, D. C.; Richardson, J. S.; Terwilliger, T. C.; Zwart, P. H., Phenix: A Comprehensive Python-Based System for Macromolecular Structure Solution. *Acta crystallographica. Section D, Biological crystallography* **2010,** *66* (Pt 2), 213-221.

47.   Emsley, P.; Cowtan, K., Coot: Model-Building Tools for Molecular Graphics. *Acta crystallographica. Section D, Biological crystallography* **2004,** *60* (Pt 12 Pt 1), 2126-2132.

48.   Joosten, R. P.; Long, F.; Murshudov, G. N.; Perrakis, A., The Pdb_Redo Server for Macromolecular Structure Model Optimization. *IUCrJ* **2014,** *1* (Pt 4), 213-220.

49.   Case, D.; Cerutti, D.; Cheatham Iii, T.; Darden, T.; Duke, R.; Giese, T.; Gohlke, H.; Goetz, A.; Greene, D.; Homeyer, N.; Izadi, S.; Kovalenko, A.; Lee, T.; LeGrand, S.; Li, P.; Lin, C.; Liu, J.; Luchko, T.; Luo, R.; Mermelstein, D.; Merz, K. M.; Monard, G.; Nguyen, H.; Omelyan, I.; Onufriev, A.; Pan, F.; Qi, R.; Roe, D. R.; Roitberg, A.; Sagui, C.; Simmerling, C.; Botello-Smith, W.; Swails, J.; Walker, R.; Wang, J.; Wolf, R.; Wu, X.; Xiao, L.; York, D.; Kollman, P., Amber 2017. *University of California, San Francisco* **2017**.

50.   Maier, J. A.; Martinez, C.; Kasavajhala, K.; Wickstrom, L.; Hauser, K. E.; Simmerling, C., Ff14sb: Improving the Accuracy of Protein Side Chain and Backbone Parameters from Ff99sb. *Journal of chemical theory and computation* **2015,** *11* (8), 3696-3713.

51.   Wang, J.; Wang, W.; Kollman, P. A.; Case, D. A., Antechamber: An Accessory Software Package for Molecular Mechanical Calculations. *J. Am. Chem. Soc* **2001,** *222*, U403.

52.   Ryckaert, J.-P.; Ciccotti, G.; Berendsen, H. J., Numerical Integration of the Cartesian Equations of Motion of a System with Constraints: Molecular Dynamics of N-Alkanes. *Journal of Computational Physics* **1977,** *23* (3), 327-341.

53.   Roe, D. R.; Cheatham III, T. E., Ptraj and Cpptraj: Software for Processing and Analysis of Molecular Dynamics Trajectory Data. *Journal of Chemical Theory and Computation* **2013,** *9* (7), 3084-3095.

54.   Humphrey, W.; Dalke, A.; Schulten, K., Vmd: Visual Molecular Dynamics. *Journal of molecular graphics* **1996,** *14* (1), 33-38.

1
2
3
4
5
6
7
8
9
10
11
12
13
14
15
16
17
18
19
20
21
22
23
24
25
26
27
28
29
30
31
32
33
34
35
36
37
38
39
40
41
42
43
44
45
46
47
48
49
50
51
52
53
54
55
56
57
58
59
60

55.   Glykos, N. M., Software News and Updates Carma: A Molecular Dynamics Analysis Program. *Journal of Computational Chemistry* **2006,** *27* (14), 1765-1768.

56.   Floyd, R. W., Algorithm 97: Shortest Path. *Communications of the ACM* **1962,** *5* (6), 345.

1
2
3
4
5
6
7
8
9
10
11
12
13
14
15
16
17
18
19
20
21
22
23
24
25
26
27
28
29
30
31
32
33
34
35
36
37
38
39
40
41
42
43
44
45
46
47
48
49
50
51
52
53
54
55
56
57
58
59
60

Table of Contents Graphic

6N EC$_{50}$ = 15.7 ± 0.8 nM

structure-guided SAR results in potent LRH-1 agonist 6N

crystal structures of three new agonists highlight novel mechanism of action

new agonist 6N demonstrates anti-inflammatory effects in intestinal organoids